sustainability

MDPI

Article

Multi-Objective Load Scheduling for Home Energy Management Considering the Thermal Behavior of the Building and User Comfort

Rodrigo Fiorotti [1,2,*], Adryanne Fazolo Nardoto Araujo [1], Helder Roberto de Oliveira Rocha [1,*], Carlos Roberto Coutinho [1,2], Lucas Freire Santos Azeredo [1] and Jussara Farias Fardin [1,*]

[1] Graduate Program in Electrical Engineering, Federal University of Espírito Santo (UFES), Vitória 29075-910, Brazil
[2] Department of Electrical Engineering, Federal Institute of Espírito Santo (IFES), São Mateus 29932-540, Brazil
* Correspondence: rodrigo.fiorotti@ifes.edu.br (R.F.); helder.rocha@ufes.br (H.R.d.O.R.); jussara.fardin@ufes.br (J.F.F.)

Abstract

Thermostatically controlled appliances are major electricity consumers in residential buildings, yet conventional home energy management systems (HEMSs) often model them as fixed-power loads, neglecting thermal dynamics. This paper presents a multi-objective HEMS that integrates the NSGA-III evolutionary algorithm with physics-based thermal models, data-driven meteorological forecasting, and electric vehicle smart charging (unidirectional, grid-to-vehicle) considering battery degradation. Air-conditioning demand is estimated using a resistance—the capacitance thermal model of the room, while tankless water-heater demand is calculated from the required temperature rise. Both models are driven by weather forecasts generated using a stacking ensemble of three deep learning models. User preferences are represented through a comfort matrix, while rooftop photovoltaic (PV) generation and hourly grid carbon emission factors are incorporated. The HEMS simultaneously minimizes daily electricity cost and CO_2 emissions while maximizing user comfort over a 24 h horizon under two time-of-use tariff schemes. The results show that under the Brazilian White Tariff, the knee-point solution reduces the daily electricity cost by 27.1% and the emissions by 28.3% with respect to a non-optimized household while keeping 90.2% of the theoretical maximum comfort; within the Pareto front, the minimum-cost solution costs 22.2% less than the maximum-comfort schedule. The minimum-emission solution reduces emissions to about 1.09 $kgCO_2eq/day$, and PV self-consumption rises from 50.7% to 94.0%, while grid import in the peak tariff block falls by 67%.

Keywords: home energy management system; artificial intelligence; thermal modeling; time-of-use tariff; electric vehicle; user comfort

Check for updates

Academic Editors: Mikaeel Ahmadi and Atsushi Yona

Received: 8 October 2026
Revised: 28 October 2026
Accepted: 3 November 2026
Published: 5 November 2026

Copyright: © 2026 by the authors. Licensee MDPI, Basel, Switzerland. This article is an open access article distributed under the terms and conditions of the Creative Commons Attribution (CC BY) license.

1. Introduction

The residential sector accounts for a substantial and growing share of electricity consumption worldwide, and the electrification of end uses combined with the expansion of distributed photovoltaic (PV) generation is reshaping the daily demand profile of low-voltage grids [1,2]. In Brazil, distributed generation has grown rapidly under net-metering rules, while time-of-use retail tariffs—locally known as the White Tariff—remain comparatively simple with a single evening peak block [3]. In this context, home energy

management systems (HEMS) that schedule household appliances in response to price signals, on-site generation and user preferences are a key enabling technology for demand-side flexibility [4–6].

A large body of work formulates residential load scheduling as a single- or multi-objective optimization problem solved with metaheuristics, mixed-integer programming or model predictive control [7–10]. However, two simplifications are still common. First, thermostatically controlled appliances—air conditioners and water heaters, which dominate the residential load in warm climates [11]—are frequently modeled as fixed-power blocks, even though their instantaneous demand depends on the outdoor temperature, the thermal inertia of the building envelope and the desired set-points [12,13]. Ignoring this coupling biases both the estimated cost of a schedule and the resulting demand profile. Second, user comfort is often reduced to allowable time windows, whereas empirical usage patterns provide a richer, probability-based description of when occupants actually prefer to run each appliance [14].

Recent studies have begun to close these gaps. Wang et al. [13] combined a resistance–capacitance (RC) building model with day-ahead appliance scheduling for PV/T-powered buildings and showed that ambient temperature dominates the indoor thermal response. Fiorotti et al. [14] introduced a comfort matrix built from historical usage frequencies and coupled thermal and electrical energy management in smart homes with photovoltaic–thermal collectors, later extending the approach to include electric-vehicle integration and emission objectives [15]. Luo et al. [16] addressed many-objective scheduling with stochastic occupant behavior. Nevertheless, the combined effect of (i) physics-based thermal load models, (ii) probability-based comfort quantification, (iii) PV self-consumption under asymmetric injection compensation, and (iv) the sensitivity of the resulting schedules to the temporal granularity of the tariff has, to the best of our knowledge, not been analyzed jointly for a single-family smart home under Brazilian regulatory conditions.

The increasing penetration of electric vehicles (EVs), driven by their potential contribution to transport-sector decarbonisation and their lower relative energy cost per kilometer traveled, is also expected to increase the electricity demand of residential buildings. As EV charging becomes increasingly integrated into residential electricity consumption, it may introduce additional demand and temporal variability into household load profiles, reinforcing the need for effective energy management strategies capable of coordinating electricity consumption with local renewable generation and user requirements [17].

This paper addresses that gap. A multi-objective HEMS is developed in which the NSGA-III evolutionary algorithm [18] schedules controllable and thermal loads over a 24 h horizon, simultaneously minimizing the daily energy cost and maximizing a comfort index derived from the Brazilian national appliance-usage survey [19]. The air conditioner is represented by a RC thermal network of the room envelope, where the wall is represented by a 3R2C model, while heat transfer through the window is represented by a thermal resistance with negligible thermal capacitance. The indoor air is represented by thermal capacitance. The resulting integrated network comprises four thermal resistances and three thermal capacitances (4R3C) with three state variables corresponding to the temperatures of the inner and outer wall layers and the indoor air [13], parameterized with construction properties representative of Brazilian dwellings [20], and the tankless water heater is modeled from the thermodynamic power required to reach the target outlet temperature given the seasonal inlet temperature. Rooftop PV generation is estimated from measured irradiance and temperature data, and the cost function follows current Brazilian net-metering rules, in which injected energy is compensated at a lower rate than consumed energy [3].

1.1. Related Works

Recent advances in HEMSs have focused on integrating photovoltaic generation, demand response, and optimization-based load scheduling to reduce energy costs, peak demand, and grid dependency while improving user comfort. Although numerous optimization techniques have been proposed, most studies model thermostatically controlled appliances as fixed-power loads and represent user comfort through simplified scheduling constraints, neglecting the influence of building thermal dynamics, weather conditions, and realistic user behavior [21]. Consequently, there remains a need for HEMS frameworks that jointly integrate physics-based thermal models, probabilistic user preferences, and multi-objective load scheduling. Therefore, this section reviews the most relevant studies, identifies the existing research gaps, and highlights the contributions of the proposed approach.

Early studies primarily focused on shifting the operation of flexible appliances under time-of-use (TOU), real-time pricing (RTP), and critical peak pricing (CPP) tariffs. For example, Laicane et al. [22] proposed a scheduling strategy for washing machines and dishwashers that reduced residential peak demand by approximately 24%. Heleno et al. [23] demonstrated that the coordinated scheduling of multiple households can provide ancillary services to the distribution network, while Abreu et al. [24] introduced the AnyPLACE platform, employing mixed-integer linear programming (MILP) to coordinate residential appliances, air-conditioning systems, and water heaters, simultaneously reducing electricity costs and increasing PV self-consumption.

Mathematical programming approaches were widely adopted in the early development of residential load scheduling. Mixed-integer linear programming (MILP) has been extensively employed because of its ability to accurately model appliance operating constraints, including minimum operating times, scheduling windows, and binary operating states [25]. For instance, Erdinc et al. [26] proposed an MILP-based HEMS under dynamic electricity pricing, demonstrating significant reductions in daily electricity costs through the coordinated scheduling of residential energy resources. Although mathematical programming methods provide optimal solutions for linear formulations, their computational complexity increases considerably as the number of decision variables, operational constraints, and nonlinear models grows, limiting their applicability to more realistic HEMS formulations.

Consequently, metaheuristic optimization algorithms have become increasingly popular for residential load scheduling due to their ability to efficiently solve highly nonlinear and combinatorial optimization problems. Algorithms such as genetic algorithms (GAs), Particle Swarm Optimization (PSO), Ant Colony Optimization (ACO), and their variants have been successfully applied to coordinate household appliances under different electricity pricing schemes [27–29]. More recently, hybrid optimization approaches combining complementary metaheuristics have been proposed to improve the balance between exploration and exploitation of the search space, leading to higher-quality solutions and faster convergence [30].

Multi-objective metaheuristics are particularly well suited for solving HEMS problems involving conflicting objectives, such as minimizing electricity costs while maximizing user comfort. Unlike single-objective optimization methods, these algorithms generate a set of non-dominated solutions, known as the Pareto front, allowing users to select the operating point that best matches their preferences. Dehghani et al. [31] proposed a multi-objective HEMS integrating photovoltaic generation and distributed energy resources, where an enhanced Biogeography-Based Optimization algorithm was employed to simultaneously minimize operating costs and maximize the load factor. Similarly, Terci-Flores et al. [32] adopted a multi-objective formulation to balance electricity cost and user comfort through

a genetic algorithm, demonstrating the effectiveness of Pareto-based optimization for residential load scheduling.

The effectiveness of any HEMS optimization algorithm strongly depends on the accuracy of the appliance models adopted. Residential loads are commonly classified into non-controllable, deferrable, and thermostatically controlled loads (TCLs). While deferrable appliances exhibit nearly constant power demand and flexible operating periods, TCLs—including air conditioners and electric water heaters—present electricity consumption that depends on weather conditions, building characteristics, and user-defined temperature set-points. Nevertheless, many existing HEMS still represent these appliances as constant-power loads, considerably simplifying the optimization problem but introducing inaccuracies in demand estimation and operating cost calculation.

To overcome this limitation, recent studies have incorporated physics-based thermal models into HEMS to more accurately represent the dynamic behavior of TCLs. Wang et al. [13] integrated a resistance–capacitance (RC) building model into a day-ahead HEMS, demonstrating that ambient temperature and the thermal inertia of the building significantly influence the energy consumption of air-conditioning systems. Similarly, Fiorotti et al. [14] proposed a multi-objective HEMS that combines an RC-based building model with a thermodynamic model of electric water heaters, enabling a more realistic estimation of the energy consumption of thermal loads. This framework was subsequently extended to incorporate additional optimization objectives while preserving the same thermal modeling approach [15].

The active scheduling of TCLs is complementary to passive improvements in the building envelope. Phase change materials (PCMs) integrated into walls, ceilings, and plasters store and release latent heat within a narrow temperature range, increasing the effective thermal capacitance of the envelope, attenuating indoor temperature swings, and delaying the peak of the cooling load [33]. Recent phase change composites combine high latent-heat storage with tunable thermal conductivity and shape stability, which broadens their use in thermal management [34]. From the HEMS perspective, PCM-enhanced envelopes and thermal insulation enlarge the time window in which the air-conditioning load can be shifted without compromising indoor comfort, because the stored cold is released when the unit is off. In a lumped RC model such as the one adopted in this work, these effects are represented by larger wall capacitances ($C_{m,in}$, $C_{m,out}$) and resistances (R_m), so that envelope retrofits and load scheduling can be co-optimized in the same framework; this possibility is discussed as future work in Section 5.

In addition to accurately modeling the physical behavior of TCLs, preserving user comfort remains one of the principal challenges in residential energy management. Early studies represented comfort through predefined operating windows or indoor temperature limits, which guarantee minimum service requirements but fail to represent occupants' habitual appliance usage. Consequently, more recent studies have formulated comfort as an explicit optimization objective. Terci-Flores et al. [32] demonstrated that simultaneously optimizing electricity cost and user comfort produces more balanced residential load schedules than purely cost-oriented formulations.

Recent research has further improved HEMSs by incorporating probabilistic and stochastic representations of occupant behavior. Rocha et al. [35] introduced a comfort matrix obtained through *k*-means clustering of appliance usage data, while Fiorotti et al. [36] proposed a probabilistic comfort model based on historical appliance usage frequencies, allowing user preferences to be naturally incorporated into the optimization process with low computational complexity. Luo et al. [16] further extended this concept by proposing a stochastic occupant behavior model based on Markov chains and the Metropolis–Hastings algorithm, explicitly distinguishing the operating characteristics of thermostatically con-

trolled and deferrable loads while accounting for the uncertainty associated with residential appliance usage.

In addition to realistic appliance and occupant modeling, the performance of day-ahead HEMSs strongly depends on the accuracy of the forecasted input variables, particularly solar irradiance, ambient temperature, and residential electricity demand. Since load scheduling decisions are computed using predicted rather than actual operating conditions, forecasting errors propagate directly to the optimization process, affecting the estimation of photovoltaic generation, thermal load consumption, electricity costs, and user comfort. Consequently, the development of accurate forecasting models has become an important research topic for improving the reliability and effectiveness of day-ahead HEMSs.

Forecasting approaches for photovoltaic generation can generally be classified into physical, statistical, and data-driven methods. While physical and statistical models have been successfully applied to day-ahead forecasting, recent studies have demonstrated that deep learning techniques, particularly Long Short-Term Memory (LSTM) networks and hybrid CNN–LSTM architectures, achieve superior predictive performance by capturing the nonlinear relationships between historical generation data and meteorological variables [37–39]. These improvements significantly reduce forecasting errors, leading to more reliable day-ahead scheduling decisions.

Although significant advances have been made in thermal load modeling, occupant behavior representation, and forecasting, these aspects are often addressed independently. Most HEMSs still simplify at least one key component, such as TCL modeling, user comfort, or forecasting uncertainty. Therefore, there remains a need for integrated HEMS frameworks that jointly combine physics-based thermal models, realistic occupant behavior, accurate day-ahead forecasting, and multi-objective optimization.

Another important gap is the consideration of battery degradation, whether in conventional or EV batteries, as it directly affects the costs and emissions associated with SHs. In this context, Dias de Lima et al. [40] proposed an MILP model for HEMS optimization considering battery cycle degradation. The model accounts for different battery operating patterns and their impacts on cycle aging while considering PV generation, energy storage, and load shifting. The results showed that the proposed HEMS can eliminate energy purchases during peak hours and achieve energy cost reductions of up to 26.56%.

With the growing adoption of EVs, using their batteries to provide flexibility to HEMSs is an increasingly promising solution, since the battery has already been acquired for mobility purposes, avoiding significant additional investment. However, this approach increases HEMS complexity because the battery can interact with the SH only when the EV is connected, the charger may support either unidirectional charging or bidirectional V2G operation, battery degradation and its associated costs and emissions must be considered, and sufficient SOC must be maintained to meet the user's mobility requirements [17]. Huy et al. [41] proposed a supervised learning-based HEMS approach to minimize energy costs through a mixed-integer linear programming (MILP) formulation. The proposed framework integrates load scheduling, battery energy storage, an EV with a bidirectional charger, and photovoltaic (PV) generation.

To the best of the authors' knowledge, no prior work simultaneously integrates physics-based building envelope RC thermal modeling, thermodynamic electric shower modeling, empirical comfort matrices derived from national survey data, and multi-horizon meteorological forecasting within a unified multi-objective evolutionary load scheduling framework. Finally, Table 1 summarizes the main characteristics of related works in the literature.

Table 1. Comparison between similar works in the literature.

Ref.	Technique	Objective Function	LS	UC	TCL	DP	PV	EV	BD
[9]	Stochastic MILP	Cost	✓	✓	✓	X	✓	X	X
[13]	MILP	Cost and peak reduction	✓	X	✓	X	✓	X	X
[14]	NSGA-III + NARX	Cost and UC	✓	✓	✓	✓	✓	X	X
[16]	NSGA-III	Cost, emissions and RI	✓	X	✓	✓	X	X	X
[22]	-	Peak reduction	✓	X	X	X	X	X	X
[23]	MILP	Flexibility and reserve	✓	✓	✓	✓	X	X	X
[25]	MILP	Cost and peak reduction	✓	X	✓	X	✓	✓	X
[26]	MILP	Cost minimization	✓	✓	✓	X	✓	✓	X
[27]	Robust optimization	Cost minimization	✓	X	X	X	X	X	X
[28]	HEM control algorithm	Cost and peak reducion	✓	✓	X	X	✓	X	X
[29]	HEMS algorithm	Cost and peak limitation	✓	✓	X	X	✓	X	X
[30]	Hybrid-integer	Cost, peak reduction and UC	✓	✓	X	X	X	X	X
[31]	IBBO	Cost and energy management	✓	X	X	X	✓	✓	X
[32]	Genetic algorithm	Cost and UC	✓	✓	X	X	✓	X	X
[35]	NSGA II	Cost and UC	✓	✓	X	✓	✓	X	X
[40]	MILP	Cost minimization	✓	X	X	X	✓	X	✓
[41]	MILP + supervised learning	Cost minimization	✓	X	X	✓	✓	✓	X
Our	**NSGA-III + Stacking**	**Cost, emissions and UC**	✓	✓	✓	✓	✓	✓	✓

LS—Load Scheduling; UC—User Comfort; TCL—Thermostatically Controlled Load; DP—Data Prediction; PV—Photovoltaic; EV—Electric Vehicle; BD—Battery Degradation; RI—Ramping Index; IBBO—Improved Biogeography-based Optimization Algorithm.

1.2. Our Contributions

To address the limitations identified in the literature, this paper proposes an advanced multi-objective home energy management system that holistically couples a physics-based thermal modeling of the building envelope and thermostatically controlled loads, data-driven multi-horizon meteorological forecasting, empirical user comfort modeling, and electric vehicle battery storage with rooftop solar PV generation. There are five main contributions of this work:

1. A tri-objective HEMS formulation that embeds physics-based RC and thermodynamic models of thermostatically controlled loads directly inside the fitness evaluation of the NSGA-III evolutionary algorithm, simultaneously optimizing daily electricity cost, occupant comfort, and greenhouse gas emissions (CO_2);
2. The integration of an interpretable multi-horizon meteorological forecasting framework based on a stacking ensemble of LSTM, TCN, and TFT deep learning architectures to feed accurate 24-step day-ahead ambient temperature and solar irradiance predictions into the thermal and PV models;
3. The coordination of electric vehicle battery storage (EVESS), operated as unidirectional smart charging (G2V), with rooftop photovoltaic generation under Brazilian Law 14300/2022 net-metering compensation rules, enabling automated peak-shaving, valley-filling, and PV self-consumption maximization;
4. A comprehensive 3D Pareto frontier and 2D projection analysis under both the Brazilian White Tariff (TOU-1) and an adapted multi-tier tariff (TOU-2), quantifying the trade-offs across four representative operating policies: Minimum Cost (S_1), Knee Point (S_2), Maximum Comfort (S_3), and Minimum Emission (S_4), complemented by a comparison with a non-optimized household operation (S_0), a comparison between NSGA-III and NSGA-II under the same computational budget, and a sensitivity analysis to tariff levels, forecast errors, and thermal parameters; and
5. Detailed empirical analysis of load-class behavior, showing that thermal loads are scheduled primarily according to comfort setpoints and outdoor thermal gradients,

while shiftable appliances and EV storage provide demand flexibility in response to price signals and emission factors.

The remainder of the paper is organized as follows. Section 2.1 details the system architecture, tariff, thermal, PV, user-behavior, and optimization models. Section 3 presents and discusses the simulation results. Section 4 discusses the practical implications and methodological limitations, while Section 5 concludes the paper and outlines future research directions.

2. Materials and Methods

2.1. System Architecture

The proposed HEMS manages the energy consumption of a single-family SH equipped with a rooftop PV generation system (P_{pv}). The household loads are classified into three categories: conventional controllable or shiftable appliances (P_c), thermostatically controlled appliances (P_t), and non-controllable loads (P_{nc}). The latter are aggregated into a single meter to reduce instrumentation complexity, as can be seen in Figure 1.

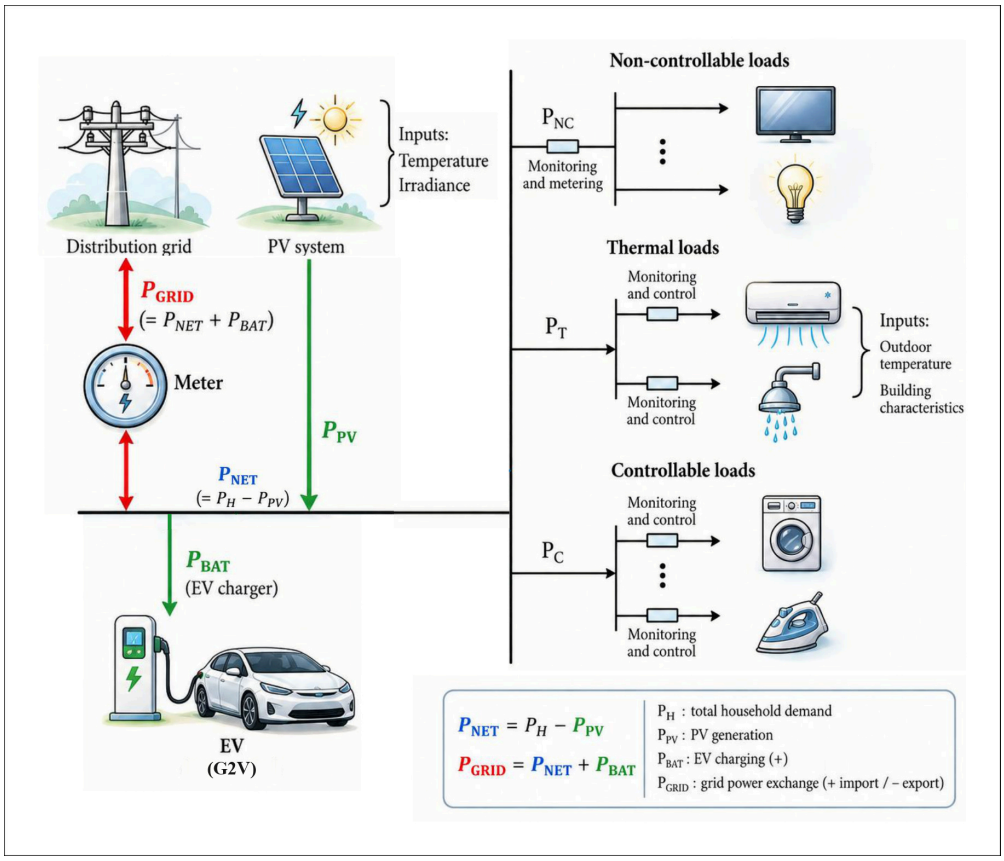


Figure 1. Architecture proposed for the HEMS. PV: photovoltaic system; P: power; SH: smart home; NC: non-controllable; T: thermal; C: controllable. The EV charger operates in unidirectional grid-to-vehicle (G2V) mode.

The SH illustrated in Figure 1 is composed of eleven electrical buses: one dedicated to the aggregated non-controllable loads and ten individually connected to the controllable and thermal appliances, enabling each schedulable device to be independently monitored and switched. The number of daily cycles and the cycle duration of each controllable appliance are listed in Table 2. All appliances are assumed to operate at constant nominal power during their cycles with the exception of the air conditioner P_{ar} and the tankless water heater P_s: being thermal loads, their power varies with the outdoor conditions and

the thermal characteristics of the building, and dedicated models (Sections 2.5.1 and 2.5.2) are embedded in the fitness evaluation.

Table 2. Load definition, nominal power (P), cycle duration (c_d), fraction of each operating hour in which the appliance draws its nominal power (p_{cd}), and number of daily cycles (n).

Appliance	Class	P (W)	c_d (h)	p_{cd}	n
AC Bedroom	Thermal	P_{ar}	6	1	1
AC Suite	Thermal	P_{ar}	8	1	1
Washing Machine	Controllable	1550	1	1	1
Electric Oven	Controllable	920	1	0.5	1
Dishwasher	Controllable	2500	1	0.25	1
Electric Iron	Controllable	1500	1	0.25	1
Clothes Dryer	Controllable	2000	1	0.5	1
Ceiling Fan	Controllable	75	6	1	1
Floor Fan	Controllable	75	6	1	1
Electric Shower	Thermal	P_s	1	0.25	5

Nominal powers and usage statistics follow the Brazilian appliance-ownership survey [19].

The parameter p_{cd} is the fraction of each scheduled one-hour interval during which the appliance actually draws its nominal power (an hourly duty factor). It does not change the number of scheduled hours, which is always $n \cdot c_d$ (Equation (34)), but it scales the energy: the energy of one cycle of a constant-power appliance is $P \cdot c_d \cdot p_{cd}$, and its mean power in a scheduled hour is $P \cdot p_{cd}$ (Equation (31)). For example, each dishwasher cycle consumes $2500 \times 1 \times 0.25 = 0.625$ kWh and each electric-oven cycle $920 \times 1 \times 0.5 = 0.46$ kWh. For the electric shower, $p_{cd} = 0.25$ means that each of the five daily showers lasts 15 min, during which the heater draws the weather-dependent power P_s of Section 2.5.2; the shower energy in a scheduled hour is therefore $0.25 \cdot P_s(i) \times 1$ h. The appliances with $c_d > 1$ (air conditioners and fans) operate for c_d consecutive hourly intervals, which may wrap around midnight (e.g., 22:00–04:00).

The optimization engine is the NSGA-III algorithm [18] formulated with three simultaneous objective functions: (i) total daily electricity cost (c_e), to be minimized; (ii) user comfort index (U_c), to be maximized; and (iii) total daily greenhouse gas emissions (E_{CO_2}), to be minimized. NSGA-III is chosen due to its structured reference-point mechanism, which maintains uniform solution spread across high-dimensional and non-convex Pareto fronts without suffering from loss of selection pressure. In NSGA-II [42], diversity is preserved by the crowding distance, which is known to lose effectiveness as the number of objectives grows, because a large share of the population becomes mutually non-dominated and the crowding distance no longer spreads the solutions uniformly along the front [18,43]; with three objectives, the problem lies at the boundary of this regime, and the two algorithms are compared under the same computational budget in Section 3.11. Each chromosome encodes the operational start times of the schedulable appliances (14 decision variables, one per daily cycle in Table 2: $9 \times 1 + 5 = 14$) and the continuous charging power trajectory of the EVESS (9 decision variables: the charging fraction P_{cd} of each of the eight 3 h periods of the day and the initial state of charge SOC_{ini}), resulting in a total of 23 decision variables ($n_{\text{var}} = 23$). Each start-time gene is a real number in $(0, 24]$ rounded up to the start interval of the cycle. Linear crossover combines parental chromosomes through random weighting factors, and Gaussian mutation perturbs selected decision variables with normally distributed perturbations. Mutated genes are constrained to the physical operating horizon of 1–24 h, ensuring feasibility across all generations.

2.2. User-Behavior Model and Comfort Matrix

User preferences are encoded following the comfort-matrix approach of Fiorotti et al. [14]. The probability that appliance j is in use during interval i is estimated from usage-frequency data of the Brazilian appliance-ownership and usage survey [19]:

$$f(i,j) = \frac{Nh_n(i,j)}{\sum_{i=1}^{N_i} Nh_n(i,j)}, \quad (1)$$

where $Nh_n(i,j)$ counts how many times appliance j was switched on in interval i and $N_i = 24$ is the number of daily intervals. Figure 2 illustrates the construction of the comfort matrix with a synthetic example.

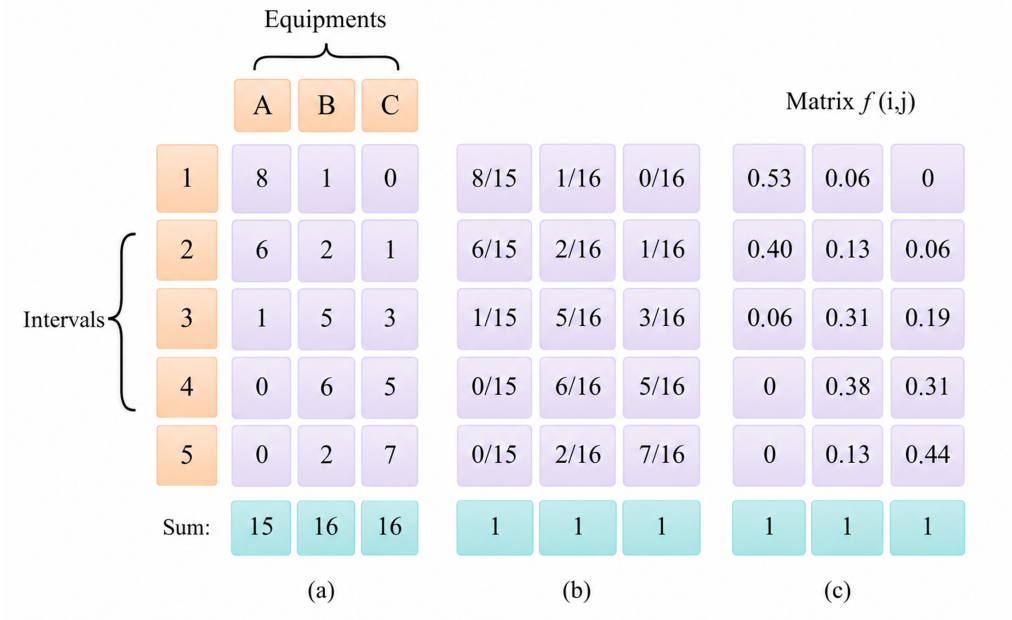


Figure 2. Methodological construction of the comfort matrix: (**a**) raw usage counts from national survey data; (**b**) frequency normalization via Equation (1); (**c**) resulting two-dimensional comfort probability profile.

Figure 3 displays the complete three-dimensional comfort matrix $f_{i,j}$ generated for all ten controllable household appliances across the 24 h of the day. The matrix encapsulates clear habit-driven usage peaks: laundry and kitchen appliances (washing machine, dishwasher, electric oven, clothes dryer) exhibit distinct morning (07:00–10:00) and evening (18:00–21:00) usage concentrations, whereas cooling appliances (air conditioners and fans) peak during late afternoon and nocturnal sleeping intervals.

The matrix $f(i,j)$ plays two distinct roles. For controllable and thermal loads, it acts as the comfort matrix, steering the optimizer toward operating hours aligned with the occupants' habits. For non-controllable loads, it is used directly as a temporal distribution profile, allocating their fixed daily consumption across the day according to the observed usage probability. In this study, the national average usage pattern of 2019 is adopted; in a real deployment, the matrix would be learned from the smart-home measurements themselves, as indicated in Figure 1, which would personalize the comfort signal without any change to the optimization framework.

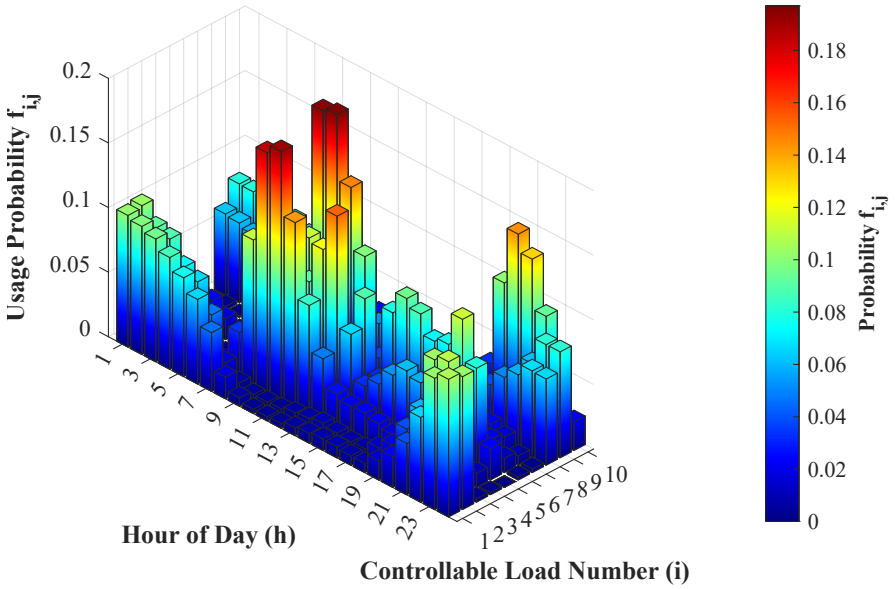


Figure 3. Three-dimensional comfort matrix showing the hourly usage probability ($f_{i,j}$) for all ten controllable residential appliances over the 24 h horizon derived from the Brazilian national appliance survey [19].

2.3. Forecasting Methodology

The data used in this study consist of hourly meteorological observations recorded by the INMET automatic weather station, located in the municipality of São Mateus, Espírito Santo, Brazil (18.676° S; 39.864° W; altitude of 28.66 m). The historical series spans from 1 January 2023 to 31 December 2025, totaling 26,304 hourly records with a continuous temporal sequence. A small fraction of the records contained missing values, which were treated as described below. The variables collected include precipitation, atmospheric pressure, global solar radiation, dry-bulb air temperature, relative humidity, wind direction and speed, and maximum wind gust. In this work, two variables were defined as forecasting targets: air temperature (°C) and global solar radiation (kW m^{-2}).

The preprocessing stage followed four sequential procedures, applied independently for each target variable, since the derived features (lags and rolling statistics) depend on the target under consideration: (i) **Temporal linear interpolation** to fill sporadic gaps, which correspond to approximately 0.3% of the records for the numerical variables; (ii) **Outlier treatment** via interquartile-range (IQR) winsorization with bounds set at 1.5 × IQR below the first quartile and above the third quartile; (iii) **Cyclical encoding** (sine/cosine) of hour-of-day and month-of-year to properly represent daily and annual seasonality without discontinuities at cycle boundaries; (iv) **Autoregressive feature construction**—lags of 1, 3, 6, 12, and 24 h and rolling statistics (mean and standard deviation) over 3, 6, and 12 h windows—computed on the target variable itself. After discarding the initial observations lost to the lag-feature generation, each resulting dataset contains 23 predictor features, including the original meteorological variables, the cyclical time components, and the autoregressive features.

The task was formulated as a multivariate, multi-step-ahead forecasting problem: given a 24 h window of past observations (containing all predictor variables), the models estimate the target variable for the subsequent 24 h (h + 1 to h + 24). All features were standardized (zero mean, unit variance) with scaling parameters estimated exclusively on the training set. The data were split strictly in chronological order—without shuffling—into 70% training, 15% validation, and 15% test subsets, preserving temporal order and preventing information leakage from the future.

Three individual models and one combination model were evaluated with the latter consisting of a **stacking ensemble** integrating the three individual models. The first model is a recurrent network composed of two stacked bidirectional LSTM [44,45] layers (48 and 24 units, respectively), which is followed by an additive attention mechanism that weighs the contribution of each time step in the input window before aggregating it into a context vector. The context vector is processed by a dense layer (GELU activation) and linearly projected onto the 24 output steps.

The second model is a Temporal Convolutional Network (TCN) [46] composed of four residual blocks with kernel size 3 and exponentially increasing dilation rates (1, 2, 4, and 8), yielding a wide receptive field while preserving temporal causality. Each block combines two dilated causal convolutions, spatial dropout, and a residual connection. The output is aggregated via global average pooling and projected onto the 24 forecast steps.

The third model is a compact adaptation of the Temporal Fusion Transformer (TFT) [47], combining a Gated Residual Network (GRN) for variable selection, an LSTM layer for local sequential modeling, and a multi-head self-attention layer for capturing long-range dependencies. The representation at the last time step, after a second GRN and layer normalization, is projected onto the 24 output steps.

The combination model follows the classical *stacked generalization* framework [48], in which the final forecast is produced by a **linear meta-learner** fitted on the base models (LSTM, TCN, TFT) predictions on the *validation* set. One independent ordinary-least-squares regression is fitted per forecast-horizon step h ($h = 1, \ldots, 24$):

$$\hat{y}[\cdot, h] = w_{\mathrm{LSTM}}[h]\, f_{\mathrm{LSTM}}[\cdot, h] + w_{\mathrm{TCN}}[h]\, f_{\mathrm{TCN}}[\cdot, h] + w_{\mathrm{TFT}}[h]\, f_{\mathrm{TFT}}[\cdot, h] + b[h] \tag{2}$$

where $f_i[\cdot, h]$ is model i's prediction for horizon h, and $w_i[h]$ and $b[h]$ are, respectively, the coefficient assigned to model i and the intercept at horizon h, which are both estimated by least squares on the validation set. At test time, the same per-horizon weights are applied to the models test-set predictions to obtain the final forecast. Because the meta-learner is linear and horizon-specific, its coefficients are directly interpretable: they quantify each model's relative contribution to the ensemble at each lead time.

All models were implemented in Keras 3/TensorFlow 2 and trained with the Adam optimizer (learning rate of 1×10^{-3}), a Huber loss ($\delta = 1.0$), and a batch size of 256 samples. Early stopping (patience of 6 epochs, monitoring validation loss, with best-weight restoration) and adaptive learning-rate reduction (factor of 0.5, patience of 3 epochs) were employed with a maximum of 25 training epochs per expert. The stacking meta-learner (Equation (2)) was fitted with ordinary least squares (scikit-learn's `LinearRegression`) on the models validation-set predictions, requiring no gradient-based training. The full pipeline preprocessing, training of the three experts, and fitting of the stacking weights was executed independently for each target variable (temperature and radiation), using the same random seed (seed $= 42$) to ensure reproducibility.

Model performance was evaluated on the test set, jointly considering all 24 steps of the forecast horizon, using four complementary metrics: **MAE** (mean absolute error), **RMSE** (root mean squared error), $\mathbf{R^2}$ (coefficient of determination), and **MAPE** (mean absolute percentage error). The best-performing model for each metric is the one that minimizes MAE, RMSE, and MAPE and maximizes R^2. The MAPE was computed over all observations as $\mathrm{MAPE} = 100\,\mathrm{mean}(|y - \hat{y}|/(|y| + \varepsilon))$ with $\varepsilon = 10^{-3}$ kW/m^2 to avoid division by zero. For solar radiation, about 44% of the test observations are night-time zeros, for which any residual error of a few W/m^2 is divided by ε, so the full-horizon MAPE of radiation is dominated by these observations. For this reason, the radiation metrics are also reported for daylight hours only, defined as the observations with measured $G \geq 0.05$ kW/m^2, together

with the weighted absolute percentage error, WAPE $= \sum |y - \hat{y}| / \sum |y|$, which does not diverge for small observed values.

2.4. Tariff Model

Two time-of-use scenarios are simulated. The first adopts the Brazilian White Tariff as published by the local utility (EDP Espírito Santo) for 2026, which defines off-peak, intermediate and peak blocks concentrated in the late afternoon and early evening (Figure 4a). The second scenario keeps the same monetary values of the three blocks but redistributes them over the day following the more segmented tariff profile of Shenzhen, China, as used by Wang et al. [13] (Figure 4b). This "adapted tariff" emulates the direction in which time-of-use pricing is expected to evolve as renewable penetration grows, and it allows the sensitivity of the scheduler to tariff granularity to be isolated from the price level itself.

The hour ranges and prices of both scenarios are listed in Table 3, where interval i denotes the local hour $[i - 1, i)$; the same convention is used for the weather, emission, and load series. In TOU-1, the peak block covers intervals 18–20 (17:00–20:00) at BRL 1.42/kWh, the intermediate block covers intervals 17 and 21 at BRL 0.96/kWh, and the remaining 19 intervals are off-peak at BRL 0.67/kWh, so that the peak-to-off-peak ratio is 2.12. Energy injected into the grid is credited at BRL 0.26/kWh in the off-peak and intermediate blocks and at BRL 0.44/kWh in the peak block.

Table 3. Time-of-use blocks and prices adopted in the simulations (BRL/kWh). The same three price levels are used in both scenarios.

Block	TOU-1 Intervals i	TOU-2 Intervals i	Consumption/Injection
Off-peak	1–16, 22–24	1–7, 24	0.67/0.26
Intermediate	17, 21	8–9, 12–13, 19–23	0.96/0.26
Peak	18–20	10–11, 14–18	1.42/0.44

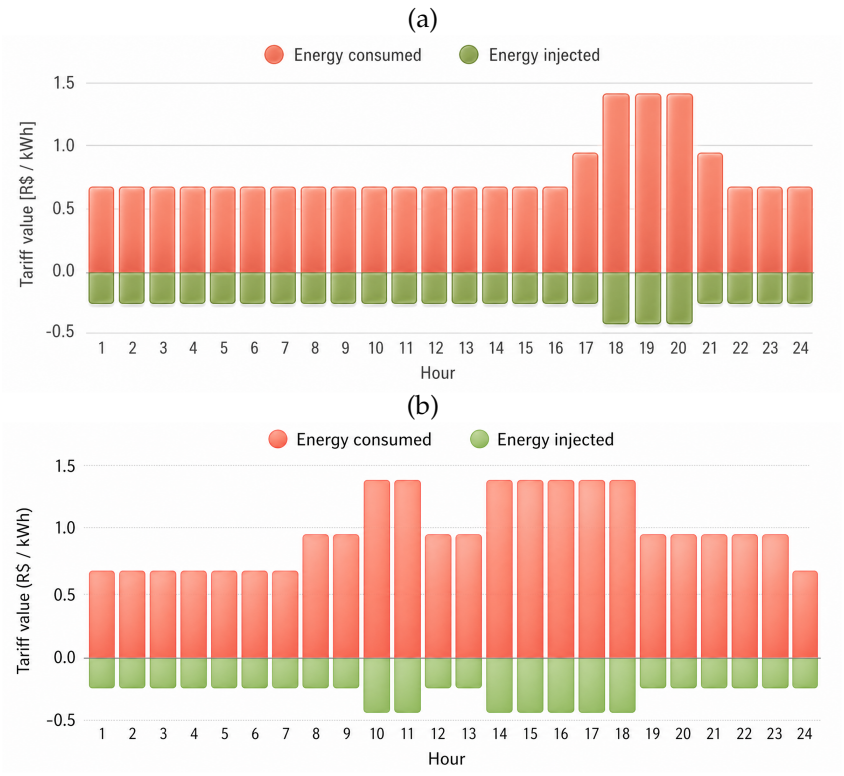


Figure 4. Hourly tariff profiles considered in the simulations: (**a**) Brazilian White Tariff (EDP Espírito Santo, 2026); (**b**) adapted tariff with the same price levels redistributed according to the Shenzhen time-of-use structure [13].

In both scenarios, the compensation rate applied to energy injected into the grid is lower than the consumption tariff. This asymmetry follows Brazilian Law 14300/2022 and ANEEL Normative Resolution 1059/2023, which progressively deduct the distribution-wire component ("Fio B") from the credits granted to prosumers [3].

2.5. Thermal Load

Thermal loads are modeled separately from conventional controllable appliances because their electrical power depends on the thermal conditions of the smart home and the user-defined comfort requirements. In the proposed HEMS, the thermal loads comprise the air conditioners and the tankless water heater, whose power consumption is determined dynamically during the evaluation of each candidate scheduling solution. Accordingly, the total thermal-load power at each time interval k is given by

$$P_t(i) = P_{ar}(i) + P_s(i), \tag{3}$$

where P_{ar} and P_s denote the electrical power consumed by the air conditioners and the tankless water heater, respectively. The following subsections describe the thermal models adopted to determine these power demands.

2.5.1. Air-Conditioner Model

The air conditioner is treated as a thermal load whose electrical demand depends on the indoor–outdoor temperature difference and on the thermal inertia of the room envelope. An RC thermal network [12,13] represents the indoor air, the inner and outer wall surfaces and the outdoor environment (Figure 5): thermal resistances describe the opposition to heat transfer across the wall, the window glazing and the convective films, while thermal capacitances describe the energy storage of the wall mass and the indoor air. The network has four thermal resistances (R_{in}, R_m, R_{out}, and R_w) and three thermal capacitances ($C_{m,in}$, $C_{m,out}$, and C_a); i.e., it is a 4R3C network whose three states are the temperatures of the two wall layers and of the indoor air; this is the network implemented and used in all results. $C_{m,in}$ and $C_{m,out}$ represent the heat stored in the inner and outer halves of the opaque wall (masonry and plaster), C_a represents the indoor air together with the light furniture of the room, R_{in} and R_{out} are the indoor and outdoor convective films, R_m is the conduction through the wall, and R_w is the direct path through the window glazing, which has negligible heat capacity. The parameter values, the initial conditions, and the COP of the unit are listed in Table 4; the heat flow Q_a in Figure 5 is the thermal power Q_{total} of Equations (4)–(7).

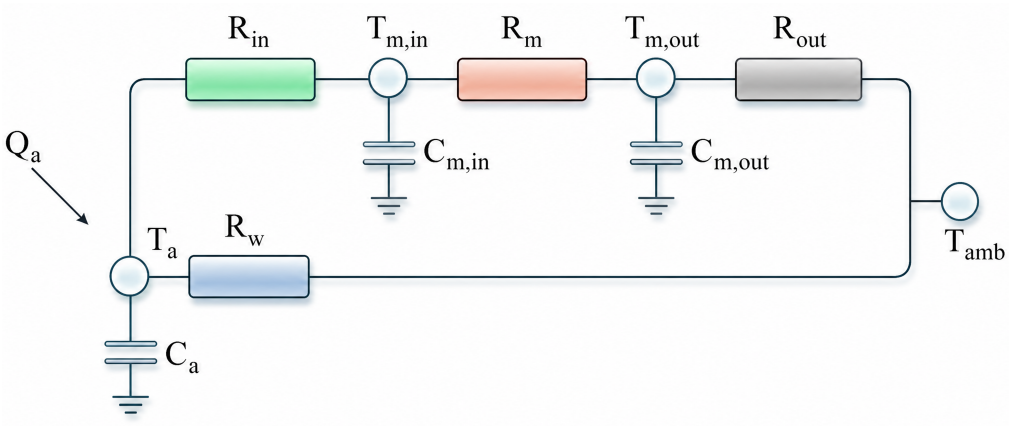


Figure 5. RC network used to model the air-conditioner energy consumption.

The electrical power of the unit is obtained from the extracted thermal power through its coefficient of performance,

$$P_{ar}(i) = \frac{Q_{total}(i)}{COP}, \tag{4}$$

and the energy balances of the two wall layers and of the indoor air are discretized with a sub-hourly time step $\Delta t = 1$ min (in Equations (5)–(7) only, where i indexes the 1-min sub-steps; elsewhere, $\Delta t = 1$ h):

$$C_{m,\text{out}} \frac{T_{m,\text{out}}(i+1) - T_{m,\text{out}}(i)}{\Delta t} = \frac{T_{\text{amb}}(i) - T_{m,\text{out}}(i)}{R_{\text{out}}} - \frac{T_{m,\text{out}}(i) - T_{m,\text{in}}(i)}{R_m}, \tag{5}$$

$$C_{m,\text{in}} \frac{T_{m,\text{in}}(i+1) - T_{m,\text{in}}(i)}{\Delta t} = \frac{T_{m,\text{out}}(i) - T_{m,\text{in}}(i)}{R_m} - \frac{T_{m,\text{in}}(i) - T_a(i)}{R_{\text{in}}}, \tag{6}$$

$$C_a \frac{T_a(i+1) - T_a(i)}{\Delta t} = \frac{T_{m,\text{in}}(i) - T_a(i)}{R_{\text{in}}} + \frac{T_{\text{amb}}(i) - T_a(i)}{R_w} - Q_{total}(i), \tag{7}$$

where $C_{m,\text{in}}$, $C_{m,\text{out}}$ and C_a are the thermal capacitances of the inner wall surface, outer wall surface and indoor air (W s K^{-1}); R_{in} and R_{out} are the convective resistances between the indoor air and the inner surface and between the outer surface and the ambient; R_m and R_w are the conductive resistances of the wall and the window glazing (K W^{-1}); $T_{m,\text{in}}$, $T_{m,\text{out}}$, T_a and T_{amb} are the inner-surface, outer-surface, indoor-air and outdoor temperatures (°C); and Q_{total} is the thermal power extracted by the air conditioner to keep the indoor air at the desired set-point, which is converted into electrical power P_{ar} through the coefficient of performance (COP) of the unit.

The optimizer, tariff, emission factor, and cost and emission objectives operate at hourly resolution, whereas the RC model uses 1-min sub-steps to maintain the numerical stability of the explicit discretization of Equations (5)–(7) and to capture the transient after each switch-on. The coupling is as follows: (i) the hourly forecast of the outdoor temperature is held constant over the 60 sub-steps of each hour; (ii) the on/off state of the air conditioner is constant within each hour and given by the candidate schedule $s_p(i, j)$; (iii) Equations (4)–(7) are integrated over the 60 sub-steps, and P_{ar} in each hour is the arithmetic mean of the 60 sub-step powers so that $P_{ar}(i) \times 1$ h is the electrical energy consumed in that hour; and (iv) the wall and air temperatures at the end of each sub-step are the initial conditions of the next one, so that the thermal inertia is carried over the whole day and is not reset at each hour. In each sub-step, Q_{total} is the heat that must be extracted to bring T_a to T_{set}, which is limited to the maximum thermal power of the unit.

Since the day represents a typical operating cycle, the simulation is designed to capture a complete 24 h cycle rather than start from arbitrary initial temperatures. It starts at the beginning of the first hour in which the unit is off after having been on, with the indoor air at the set-point, covers the 24 h, and ends in the interval preceding the starting one on the next day. The cycle is then repeated, starting from the final state of the previous cycle, until the initial and final temperatures coincide (periodic steady state, reached in a few cycles), which also closes the wall temperatures. Because the operating block of each unit is contiguous, each air conditioner has only 24 possible plans (one per start interval); their power profiles are computed once and reused in the fitness evaluation, which gives the same result as simulating every candidate.

Solar radiation on the envelope is deliberately neglected. The sensitivity analysis of Wang et al. [13] shows that the ambient temperature is by far the dominant driver of the indoor thermal response with solar gains playing a secondary role; omitting them simplifies the model and is less restrictive here than in daytime-cooled buildings, because in the schedules obtained, the air conditioners operate mainly at night (Figure 11), when solar gains are absent and only the heat stored in the walls during the day is released

through $C_{m,in}$ and $C_{m,out}$. Its effect was nevertheless quantified by adding a solar gain to the air node of Equation (7) and an absorbed flux to the outer wall node of Equation (5) (Section 3.12), and this simplification is revisited in Section 4.3.

Table 4. Parameters of the 4R3C model and air-conditioner data, identical for the bedroom and the suite (envelope values from [20]).

Parameter	Value	Unit
R_{in}, R_{out}	13.75	K/W
R_m	5.47	K/W
R_w (4-mm glazing)	0.0033	K/W
$C_{m,in}$, $C_{m,out}$	5.489×10^6	J/K
C_a	2.160×10^6	J/K
Set-point T_{set}	18	°C
Initial condition	$T_a = T_{set}$ after switch-off; periodic steady state	–
Maximum electrical power	1300	W
Rated COP (ISO 5151, condition T1)	2.9	–
Maximum thermal power	3770	W
Time step Δt	60	s

The thermal power Q_{total} required to hold the set-point is converted into electrical power P_{ar} through the coefficient of performance (COP) of the unit. A constant rated COP is adopted. The rated value refers to an outdoor temperature of 35 °C (ISO 5151, condition T1 [49]), whereas the outdoor temperature in the hours in which the units operate (at night) ranges from 19.7 to 21.0 °C; since the COP of split units increases as the outdoor temperature decreases, the constant rated COP tends to overestimate P_{ar} rather than underestimate it. The magnitude of this approximation is bounded in Section 3.12. The envelope parameters (wall and glazing resistances and capacitances) were obtained from the Projeteee platform of the Brazilian Ministry of the Environment, which provides thermal properties of construction assemblies representative of Brazilian dwellings [20]. Figure 6 summarizes the computation: the inputs are the outdoor temperature series, the binary 24-position operating plan produced by the optimizer, and the envelope parameters; the output is the estimated electrical power of the air conditioner in each interval of the evaluated schedule.

2.5.2. Tankless Water-Heater Model

Water heating is provided by an electric tankless heater, which was adopted because this type of equipment allows the desired shower temperature to be specified and adjusts its power accordingly. To determine the thermal power required to heat the water, the classical thermodynamic energy balance is used:

$$Q_{\mathrm{s}} = \dot{m}\, c_p (T_{\mathrm{out}} - T_{\mathrm{in}}), \tag{8}$$

where $\dot{m}$ is the water mass flow rate (kg s^{-1}), c_p is the specific heat of water, adopted as 4180 J kg^{-1} °C^{-1}, and T_{out} and T_{in} are the water outlet and inlet temperatures, respectively. The mass flow rate is related to the volumetric flow rate according to

$$\dot{m} = \frac{\rho\, \dot{V}}{60{,}000}, \tag{9}$$

where $\dot{V}$ is the volumetric flow rate in L/min and ρ is the water density, which is assumed to be 1000 kg m^{-3}.

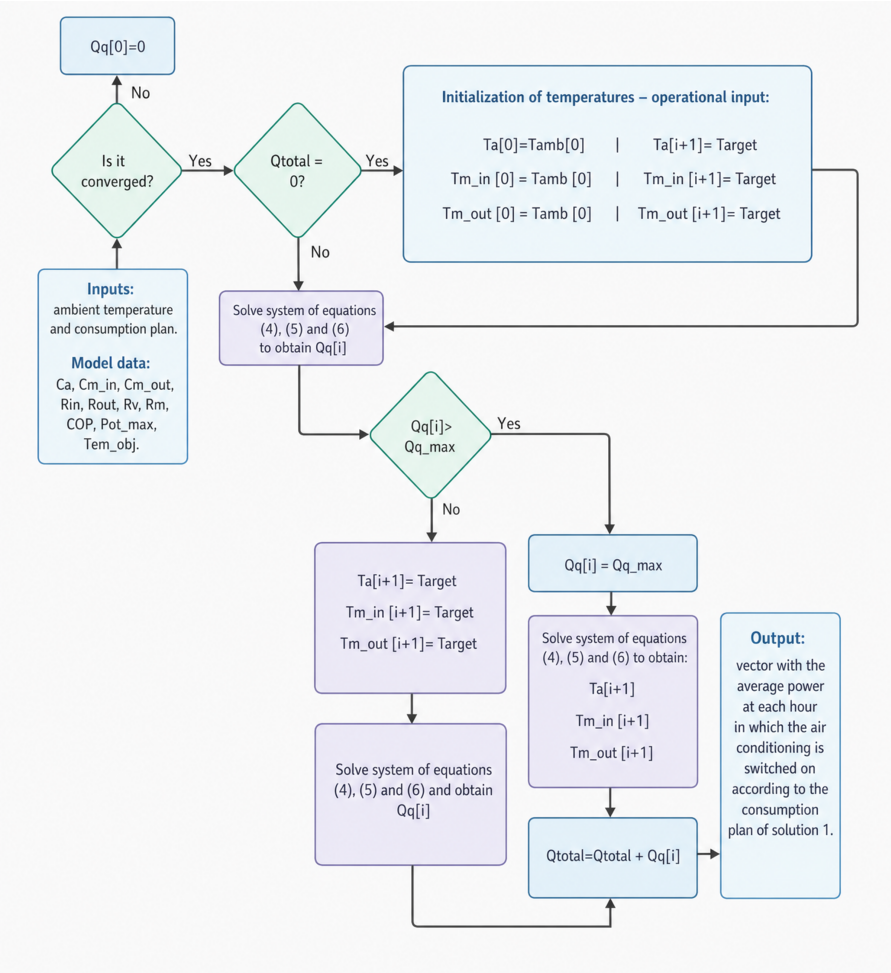


Figure 6. Flowchart of the air-conditioner model embedded in the fitness evaluation.

Because heat losses occur along the pipe connecting the tankless heater to the shower, the thermal power required to heat the water to the desired shower temperature must be distinguished from the total thermal power supplied by the heater. The useful heating power is given by

$$Q_{\text{heating}} = \dot{m}\, c_p (T_{\text{sh}} - T_{\text{in}}), \tag{10}$$

where T_{sh} is the desired water temperature at the point of consumption. The thermal power lost to the surroundings through the pipe is calculated as [13]

$$Q_{\text{loss}} = U A_{\text{pipe}} \left(T_{\text{avg}} - T_{\text{amb}}\right), \tag{11}$$

where U is the overall heat-transfer coefficient ($\text{W m}^{-2}\,\text{K}^{-1}$), A_{pipe} is the external surface area of the pipe, T_{avg} is the average water temperature, and T_{amb} is the ambient temperature. In the implementation, the loss is evaluated between the heater outlet temperature and the inlet-water temperature, $Q_{loss} = UA_{pipe}(T_{out} - T_{in})$, i.e., the inlet water (at $T_{amb} - 2\,^{\circ}\text{C}$, see below) is taken as the temperature of the surroundings of the pipe with $U = 1.69\ \text{W/m}^2\text{K}$, $A_{pipe} = 2.65\ \text{m}^2$, and $\dot{m} = 0.05\ \text{kg/s}$ (3 L/min). Combined with Equation (19), this gives $T_{out} = (\dot{m}c_p T_{sh} - UA_{pipe}T_{in})/(\dot{m}c_p - UA_{pipe})$. The overall heat-transfer coefficient is determined from the thermal resistances associated with conduction and convection. For the cylindrical pipe wall, the conductive thermal resistance is given by [50]

$$R_{\text{cond}} = \frac{\ln(r_2/r_1)}{2\pi k L}, \tag{12}$$

where r_1 and r_2 are the inner and outer radii of the cylindrical layer, respectively, k is the thermal conductivity of the material ($\mathrm{W\,m^{-1}\,K^{-1}}$), and L is the pipe length (m). The convective thermal resistance is expressed as [50]

$$R_{\mathrm{conv}} = \frac{1}{hA}, \tag{13}$$

where h is the convective heat-transfer coefficient ($\mathrm{W\,m^{-2}\,K^{-1}}$) and A is the corresponding heat-transfer area.

Thermal insulation is considered around the pipe to reduce heat losses from the hot water to the surrounding environment. The thermal conductivity of the pipe and insulation materials can be obtained from manufacturer data. The internal convective heat-transfer coefficient is estimated using the Dittus–Boelter correlation, which is applicable to turbulent flow in pipes [51]:

$$Nu_D = 0.023 Re^{0.8} Pr^n, \tag{14}$$

where Nu_D is the Nusselt number, Re is the Reynolds number, Pr is the Prandtl number, and $n = 0.3$ is adopted when the fluid is being cooled. The Reynolds number is calculated as [50]

$$Re = \frac{\rho v D}{\mu}, \tag{15}$$

where ρ is the fluid density ($\mathrm{kg\,m^{-3}}$), v is the mean fluid velocity ($\mathrm{m\,s^{-1}}$), D is the pipe diameter (m), and μ is the dynamic viscosity of the fluid (Pa s). For the operating conditions considered in this study, the Reynolds number is 4412, characterizing the flow as turbulent and therefore supporting the use of the Dittus–Boelter correlation.

The internal convective heat-transfer coefficient is obtained from the Nusselt number as [50]

$$h = \frac{Nu_D\, k_f}{D}, \tag{16}$$

where k_f is the thermal conductivity of the fluid ($\mathrm{W\,m^{-1}\,K}$). The total thermal resistance between the hot water and the ambient environment is then expressed as [50]

$$R_{\mathrm{total}} = \frac{1}{h_{\mathrm{in}} A_{\mathrm{in}}} + \frac{\ln(r_2/r_1)}{2\pi k_{\mathrm{pipe}} L} + \frac{\ln(r_3/r_2)}{2\pi k_{\mathrm{ins}} L} + \frac{1}{h_{\mathrm{out}} A_{\mathrm{out}}}, \tag{17}$$

where the first term represents internal convection, the intermediate terms account for conduction through the pipe wall and thermal insulation, and the last term represents external convection to the ambient air. The overall heat-transfer coefficient is related to the total thermal resistance by

$$U = \frac{1}{R_{\mathrm{total}} A_{\mathrm{ref}}}, \tag{18}$$

where A_{ref} is the reference heat-transfer area.

The total thermal power supplied by the tankless heater must compensate for both the useful heating demand and the thermal losses along the pipe. Therefore,

$$Q_{\mathrm{s}} = Q_{\mathrm{heating}} + Q_{\mathrm{loss}}. \tag{19}$$

Consequently, the outlet temperature of the tankless heater can be determined such that after the thermal losses along the pipe, the water reaches the desired shower temperature at the point of consumption:

$$T_{\mathrm{out}} = T_{\mathrm{in}} + \frac{Q_{\mathrm{heating}} + Q_{\mathrm{loss}}}{\dot{m}\, c_p}. \tag{20}$$

Finally, the electrical power required by the tankless heater is related to the total thermal power through the heating efficiency η_s:

$$P_s = \frac{Q_s}{\eta_s}. \tag{21}$$

For the resistive heating element considered in this study, $\eta_s = 0.95$, $T_{sh} = 40\ ^\circ\text{C}$, and the power is limited to the 8.2 kW rating of the heater. The inlet water temperature is assumed to be 2 °C lower than the ambient temperature, following the approximation proposed by [51]. Thus, the electrical power required by the tankless heater varies with the water flow rate, ambient temperature, desired shower temperature, and thermal losses along the distribution pipe.

2.6. Photovoltaic System

The PV output is estimated using a simplified irradiance/temperature-dependent power model

$$P_{\text{pv}} = N_m\, P_n\, \frac{G_i}{G_{\text{ref}}}[1 + \beta(T_c - T_{\text{ref}})], \tag{22}$$

with $\beta = -0.29\%/^\circ\text{C}$ (negative, so that the output decreases as the cell heats up) and $T_c = T_{amb} + 0.03\, G_i$ (°C, with G_i in W/m^2), where P_n is the nominal module power, $G_{\text{ref}} = 1000\ \text{W m}^{-2}$ and $T_{\text{ref}} = 25\ ^\circ\text{C}$ are the standard test conditions, N_m is the number of modules, G_i is the in-plane irradiance, β is the module temperature coefficient and T_c is the cell temperature. Six modules of 590 W each are considered ($N_m = 6$), and the irradiance and temperature series are forecast from measurements collected at a meteorological station in São Mateus, Espírito Santo, Brazil, ensuring consistency between the weather inputs used to derive the PV generation profile and thermal-load models. The resulting 3.54 kWp array generates 18.9 kWh on the simulated day, about 61% of the daily consumption of the household including the EV (30.8 kWh in the knee-point schedule); i.e., it is sized below the consumption. Under Law 14300/2022, the energy injected in excess of consumption is credited at a reduced value, so residential systems are usually sized not to exceed the consumption; even so, the array exports energy around noon on sunny days when the loads are not coordinated (9.3 kWh in the non-optimized reference of Section 3), which is the condition in which the coordination of shiftable loads and EV charging with the PV surplus is relevant.

2.7. Electric Vehicle Energy Storage System

In the context of an HEMS, the EV battery should be charged to optimize the objective functions defined in the optimization problem formulation. Since the consumption and generation profiles, electricity tariff, and objective functions may vary across different case studies, the energy management strategy should be sufficiently robust to cope with these variations. In addition, certain operational constraints must be satisfied to extend the battery lifetime and ensure safe operation. The state of charge (SOC) of the battery represents the percentage of stored energy relative to its nominal capacity (C_{bat}) and is defined by Equation (23) [52].

$$SOC(i) = (1 - \sigma) \cdot SOC(i-1) + \frac{\Delta t \cdot (\eta_{ch} \cdot P_{bat}(i) - P_{ope}(i))}{C_{bat}} \tag{23}$$

In this formulation, P_{bat} denotes the power at the charger responsible for charging the battery, while P_{ope} represents the power consumed by the EV during its trips. The parameter η_{ch} is the charging efficiency of the battery; since the charger is unidirectional, the round-

trip efficiency η_{rt}, which would affect only the discharge, does not enter Equation (23). The parameter σ denotes the battery self-discharge rate and C_{bat} is the nominal battery capacity.

The SOC must remain within a specified range, bounded by the minimum (SOC_{min}) and maximum (SOC_{max}) values, as expressed in Equation (24). Meanwhile, the EV charging power $P_{bat}(i)$ must be constrained by the maximum allowable power P_{batmax}, as described in Equation (25), which depends on the characteristics of the battery and the charger used.

$$SOC_{min} \cdot SOH(i) \leq SOC(i) \leq SOC_{max} \cdot SOH(i) \tag{24}$$

$$0 \leq P_{bat}(i) \leq P_{batmax} \cdot (1 - EV_{op}(i)) \tag{25}$$

Because $P_{bat}(i) \geq 0$, the charger is unidirectional: the EV battery is charged from the grid or from PV surplus (G2V), but it does not discharge to the house (V2H) or to the grid (V2G). The flexibility provided by the EV is therefore the shifting of its charging energy in time rather than the supply of the evening load. Here, $EV_{op}(i)$ is a variable that indicates whether the EV is traveling ($EV_{op}(i) = 1$) or connected to the charger ($EV_{op}(i) = 0$). When $EV_{op}(i) = 1$, the EV is unavailable for charging, and the term $(1 - EV_{op}(i))$ in Equation (25) forces $P_{bat}(i)$ to zero. Conversely, when $EV_{op}(i) = 0$, the EV is connected to the charger and can be charged subject to the maximum allowable power P_{batmax}.

In addition, this model accounts for battery degradation through the state of health (SOH), which is defined as the ratio between the current battery capacity and its original capacity. Factors such as charge and discharge cycles, battery lifetime, and operating temperature can significantly affect the degradation process. The SOH is determined based on the total battery aging (AGE_{tot}), as presented in Equation (26), which is calculated as the sum of two components: calendar aging (AGE_{cal}), associated with the passage of time, and cycle aging (AGE_{cyc}), associated with charge and discharge cycles, as described in Equation (27) [52].

$$SOH(i) = SOH(i-1) - (SOH_i - SOH_f) \cdot AGE_{tot}(i) \tag{26}$$

$$SOH(i) = SOH(i-1) - 0.2 \cdot (AGE_{cal}(i) + AGE_{cyc}(i)) \tag{27}$$

where SOH_i and SOH_f represent the SOH values of a new battery and a battery after undergoing $L^{80\%}cyc$ complete cycles, respectively, which are typically assumed to be 100% and 80%. The calculation of $AGEcyc$ is described in Equation (28), while AGE_{cal} is defined in Equation (29) [52].

$$AGE_{cyc}(i) = 0.5 \cdot \Delta t \cdot \frac{\eta_{ch} \cdot P_{bat}(i) + P_{ope}(i)}{L_{cyc}^{80\%} \cdot C_{bat}} \tag{28}$$

$$AGE_{cal}(i) = (6.6148 \cdot 10^{-6} \cdot SOC(i) + 4.6404 \cdot 10^{-6}) \cdot \Delta t \tag{29}$$

where $L_{cyc}^{80\%}$ represents the number of equivalent full cycles required for the battery SOH to reach 80%.

Once the battery operating constraints that must be satisfied by the HEMS have been defined, Algorithm 1 presents the EVESS strategy and its 3 operating modes, which determine the EV charging profile. The execution of this strategy is governed by the following variables: SOC and P_{net}, previously described; SOC_{ini}, which represents the initial battery SOC and is itself a decision variable, limited to $[SOC_{min}, SOC_{max}]$, so that the optimizer chooses the state of charge at the beginning of the day and the penalty of Equation (42) drives the battery back to it at the end of the day; and P_{cd}, another decision vector defined by the metaheuristic, corresponding to the fraction of P_{max} used to charge

the battery in each period p (eight periods of 3 h). Thus, $P_{cd} = 1$ corresponds to 100% of the maximum charging power, whereas $P_{cd} = 0$ indicates that the battery is not charged.

The EVESS operating strategy is implemented through three operating modes. When $EV_{op}(i) = 1$, the *CarInOperation* mode is activated, indicating that the EV is traveling and is therefore unavailable for charging. Consequently, $P_{bat}(i) = 0$, while the energy required for vehicle operation (P_{ope}) is deducted from the battery SOC, as defined in Equation (23). When the EV is connected to the charger, i.e., $EV_{op}(i) = 0$, the strategy evaluates the net power condition. If $P_{net}(i) < 0$, indicating excess power available in the SH, the *ExcessBatteryCharge* mode is activated, allowing the EV battery to be charged using the available surplus energy. Otherwise, the *BatteryCharge* mode is activated, and the optimization algorithm determines the charging power through the decision variable P_{cd}. After the operating mode is determined, the battery SOC and SOH are updated, and the procedure is repeated for the next time interval until the end of the scheduling horizon.

Algorithm 1 EVESS Operating Strategy

Require: $P_{net}(i)$, p, $EV_{op}(i)$, E_{con}, P_{cd}, SOH_{ini}, and SOC_{ini}
Ensure: $P_{bat}(i)$, $SOC(i)$, and $SOH(i)$
Initialize $i \leftarrow 1$
while $i \leq N_i$ **do**
  if $EV_{op}(i) = 1$ **then**
    Activate *CarInOperation* mode
    $P_{bat}(i) \leftarrow 0$
  else
    if $P_{net}(i) < 0$ **then**
      Activate *ExcessBatteryCharge* mode
    else
      Activate *BatteryCharge* mode
    end if
  end if
  Update $SOC(i)$ and $SOH(i)$
  $i \leftarrow i + 1$
end while
return P_{bat}, SOC, and SOH

To ensure the reproducibility of the proposed HEMS, the main parameters of the EV battery and charger adopted in the simulations are explicitly defined. The EV battery has a nominal capacity of $C_{bat} = 40$ kWh. The allowable state-of-charge range is defined between $SOC_{min} = 40\%$ and $SOC_{max} = 95\%$ with the minimum value being adopted as a mobility reserve to ensure sufficient energy for vehicle operation. The initial state of health is set to $SOH_{ini} = 100\%$, while the end-of-life condition is defined as $SOH_{eol} = 75\%$. The charging efficiency is $\eta_{ch} = 98\%$. The battery self-discharge rate is $\sigma = 0.02\%$/day. The battery cycle life is assumed to be $L_{cyc}^{80\%} = 10{,}000$ equivalent full cycles, corresponding to the number of cycles required for the battery SOH to decrease to 80%. The battery replacement cost is assumed to be $C_{inv} = 800$ RS$/kWh. The maximum charging power is set to $P_{bat}^{max} = 8$ kW. The EV is assumed to be in operation from 06:00 to 11:00 (intervals 7–11), covering a daily distance of 70 km, and the corresponding energy is drawn uniformly over these five intervals. With an energy consumption of 0.164 kWh/km, the vehicle requires approximately 11.48 kWh of energy per day. This energy requirement is considered in the EVESS model to ensure that the battery maintains the required energy reserve for the EV operation period.

2.8. Optimization Problem

2.8.1. Power Balance and Constraints

The hourly consumption of the non-controllable loads is

$$P_{nc}(i) = \sum_{x=1}^{N_{nc}} c_d(x)\, p_{cd}(x)\, n(x)\, P_{n,nc}(x)\, f(i,x), \tag{30}$$

where $P_{n,nc}(x)$ is the nominal power of non-controllable appliance x, $n(x)$ its number of daily cycles, $c_d(x)$ the cycle duration and N_{nc} the number of non-controllable appliances. Equation (30) preserves the total daily energy of these loads while distributing it according to the usage probability, and it is not affected by the optimizer.

The hourly consumption of the schedulable (controllable) loads is

$$P_c(i) = \sum_{j=1}^{N_c} P_{n,c}(j)\, s_p(i,j)\, p_{cd}(j), \tag{31}$$

where s_p is the binary scheduling matrix produced by the algorithm ($s_p(i,j) = 1$ when appliance j operates in interval i) and N_c is the number of shiftable (constant-power) schedulable appliances, i.e., the $N_c = 7$ appliances of class "Controllable" in Table 2. The $N_t = 3$ thermal appliances (the two air conditioners and the electric shower) are also scheduled by the optimizer, through the same matrix $s_p(i,j)$ for $j = N_c + 1, \ldots, N_c + N_t$, but they are excluded from Equation (31): their weather-dependent power is returned by the models of Sections 2.5.1 and 2.5.2, which are evaluated on the candidate schedule, and enters the balance only through $P_t(i) = P_{ar}(i) + P_s(i)$ (Equation (3)), where P_{ar} is the sum of the powers of the two air conditioners. The total smart-home demand is

$$P_h(i) = P_{nc}(i) + P_c(i) + P_t(i), \tag{32}$$

where the power of the thermal loads P_t is defined by the sum of P_{ar} and P_s, so each appliance is counted exactly once: the shiftable appliances in P_c, the thermal appliances in P_t, and the remaining household loads in P_{nc}.

The schedule must satisfy

$$sp(i,j) \in \{0,1\} \quad \forall i,j, \tag{33}$$

$$\sum_{i=1}^{N_i} s_p(i,j) = n(j)\, c_d(j), \tag{34}$$

$$i \in \{1,2,\ldots,24\}, \tag{35}$$

$$j \in \{1,2,\ldots,N_c + N_t\}, \tag{36}$$

where constraint (33) prevents multiple activations of the same appliance in one interval and constraint (34) enforces the user-defined number and duration of cycles for every appliance. For the electric shower, the only appliance with more than one daily cycle, constraint (33) implies that the five showers are assigned to different intervals.

With the SH power consumption and photovoltaic system generation determined, the net power of the SH is defined by Equation (37)

$$P_{net}(i) = P_h(i) - P_{pv}(i), \tag{37}$$

Finally, after the EV charger management, the power exchanged with the distribution grid, either consumed from or injected into the grid (P_{grid}), is defined by Equation (38)

$$P_{grid}(i) = P_{net}(i) + P_{bat}(i) \tag{38}$$

2.8.2. Objective Functions

The multi-objective optimization model simultaneously considers three conflicting operational criteria:

1. Daily SH Operation Cost (c_e): The daily SH operation cost is divided into four components: the energy consumption cost (c_{con}), which is calculated according to the TOU tariff (t_{tou}) described in Equation (39); the revenue from energy injection (c_{inj}) into the grid, which is calculated using the feed-in tariff (t_{fi}) in Equation (40); the battery degradation cost (c_{deg}), which is defined in Equation (41); and a penalty cost (c_p), defined in Equation (42), which is included to discourage variations in the battery energy level at the beginning and end of the day.

$$c_{\text{con}} = \sum_{i=1}^{N_i} \max\left(P_{\text{grid}}(i), 0\right) \cdot t_{tou}(i) \cdot \Delta t, \tag{39}$$

$$c_{\text{inj}} = \sum_{i=1}^{N_i} \min\left(P_{\text{grid}}(i), 0\right) \cdot t_{fi}(i) \cdot \Delta t, \tag{40}$$

$$c_{deg} = \frac{SOH_{ini} - SOH(N_i)}{1 - SOH_{eol}} \cdot C_{bat} \cdot C_{inv} \tag{41}$$

$$c_p = \begin{cases} t_{fi} \cdot (SOC_{ini} - SOC(N_i)) \cdot C_{bat} & \text{if } SOC(N_i) > SOC_{ini} \\ max(t_{tou}) \cdot (SOC_{ini} - SOC(N_i)) \cdot C_{bat} & \text{if } SOC_(N_i) \leq SOC_{ini} \end{cases} \tag{42}$$

$$c_e = c_{\text{con}} + c_{\text{inj}} + c_{deg} + c_p \tag{43}$$

where SOH_{eol} represents the battery SOH at the end of its useful life, and C_{inv} corresponds to the investment required for battery replacement per kWh.

2. Occupant Comfort Index (U_c): The comfort metric evaluates how well the scheduled appliance operating intervals align with the occupant's historical preference probabilities:

$$U_c = \sum_{j=1}^{N_c+N_t} \frac{\sum_{i=1}^{N_i} f(i,j)\, s_p(i,j)}{\sum_{i=1}^{N_i} s_p(i,j)}, \tag{44}$$

where $N_c + N_t = 10$ is the number of controllable and thermal appliances, and $f(i,j)$ is the probability extracted from the comfort matrix.

Each term of Equation (44) is the mean usage probability of appliance j over the $n(j)\, c_d(j)$ intervals in which it is scheduled; the denominator normalizes each term by the number of scheduled intervals—not by the sum of f over the day. Since $f(\cdot, j)$ sums to one over the 24 intervals (Equation (1)), each term lies between $\min_i f(i,j)$ and the mean of the $n(j)\, c_d(j)$ largest values of $f(\cdot, j)$, and U_c is the sum of ten such terms. Therefore U_c is not normalized to one: its range is $0 \leq U_c \leq U_c^{max}$, where

$$U_c^{max} = \sum_{j=1}^{N_c+N_t} \frac{1}{n(j)\, c_d(j)} \sum_{k=1}^{n(j)\, c_d(j)} f_{(k)}(j), \tag{45}$$

and $f_{(k)}(j)$ is the k-th largest value of $f(\cdot, j)$. For the comfort matrix of Figure 3, $U_c^{max} = 1.1982$, both with and without the requirement of consecutive hours for the appliances with $c_d > 1$ (their best windows are already contiguous). Values of U_c above one, such as those in Table 8, are therefore expected. Throughout the paper, comfort per-

centages are given either relative to the maximum-comfort solution found on the Pareto front (S_3) or relative to U_c^{max}, as indicated; for example, the knee point under TOU-1 retains $U_c(S_2)/U_c(S_3) = 1.0806/1.1770 = 91.8\%$ of the comfort of S_3 and $1.0806/U_c^{max} = 90.2\%$ of the theoretical bound.

U_c measures only the agreement between the operating times and the occupants' habits (preference comfort). Thermal comfort, i.e., the indoor temperature, is not part of U_c: it is enforced as a requirement in the air-conditioner model, which keeps T_a at the set-point T_{set} whenever the unit is scheduled, and in the water-heater model, which delivers water at T_{sh} in every shower. A schedule with low U_c therefore does not imply thermal discomfort during the scheduled hours but rather operation of the appliances at hours that the occupants use less often.

3. Daily CO_2 Emissions (E_{CO_2}): Similar to the operation cost, the daily SH operation emissions are divided into three components: the emissions associated with energy consumption (E_{con}), which are calculated using the hourly emission factor (E_{f}) of the Brazilian National Interconnected System (SIN) [53], as described in Equation (46), which is set to zero when energy is injected into the grid; the emissions associated with battery degradation (E_{deg}), which are defined in Equation (47); and a penalty term (E_p), which is defined in Equation (48). The emission factor is not a single annual value: $E_f(i)$ is a 24-value hourly profile obtained by averaging, for each local hour of the day (UTC–3), the 8760 hourly values of the direct carbon intensity of the SIN reported by Electricity Maps for 2023 [53]. It ranges from 0.0461 $kgCO_2eq/kWh$ in interval 20 (19:00–20:00) to 0.0580 $kgCO_2eq/kWh$ in interval 5 (04:00–05:00), i.e., about $\pm 11\%$ around its daily mean: in 2023, the Brazilian grid was most carbon intensive before dawn and least in the evening. This profile is an average (attributional) intensity of a representative day rather than the marginal intensity of the hour; the implications of this choice are discussed in Section 4.3.

$$E_{\text{con}} = \sum_{i=1}^{N_i} \max\left(P_{\text{grid}}(i), 0\right) \cdot E_{\text{f}}(i) \cdot \Delta t, \tag{46}$$

$$E_{deg} = \frac{SOH_{ini} - SOH(N_i)}{1 - SOH_{eol}} \cdot C_{bat} \cdot E_{bat} \tag{47}$$

$$E_p = \begin{cases} min(E_f) \cdot (SOC_{ini} - SOC(N_i)) \cdot C_{bat} & \text{if } SOC(N_i) > SOC_{ini} \\ max(E_f) \cdot (SOC_{ini} - SOC(N_i)) \cdot C_{bat} & \text{if } SOC(N_i) \leq SOC_{ini} \end{cases} \tag{48}$$

$$E_{CO_2} = E_{\text{con}} + E_{deg} + E_p \tag{49}$$

where E_{bat} represents the emissions associated with the battery over its entire life cycle per kWh of installed capacity.

The overall tri-objective optimization problem is formally stated as

$$\min\left\{c_e,\ -U_c,\ E_{CO_2}\right\} \tag{50}$$

subject to constraints of SH load scheduling (33)–(38), EV battery modeling (23)–(29) and EVESS operating strategy.

2.8.3. Algorithm Settings and Consistency Analysis

The NSGA-III was implemented in MATLAB (R2016a) with a population of 250 individuals evolved for 200 generations, a crossover rate of 70% and mutation applied to 30% of the population with a per-gene probability of 5%, and 231 reference points (20 divisions per objective). Constraint (33) and the lower SOC limit of Equation (24) are enforced by penalties: a schedule in which two cycles of the same appliance overlap, or in which the

SOC falls below 0.99 SOC_{min}, has BRL 1000 added to its cost, 5 subtracted from its comfort index, and 20 $kgCO_2eq$ added to its emissions, so that it is dominated by any feasible schedule. Because genetic algorithms are stochastic, a consistency analysis was performed by repeating the optimization with ten independent random seeds for each tariff; the resulting Pareto fronts were similar in shape and position, indicating that the reported fronts are representative and not artifacts of a single fortunate run. Across these runs, the maximum comfort index ranged from 1.1225 to 1.1945 under TOU-1 and from 1.1556 to 1.1915 under TOU-2, and the hypervolume of the normalized front had a coefficient of variation of 3.5% (TOU-1) and 1.8% (TOU-2). The comfort objective does not depend on the tariff, so the theoretical maximum $U_c^{max} = 1.1982$ (Equation (45)) is the same in both scenarios; the different values of S_3 in Table 8 (1.1770 and 1.1755) reflect the stochastic approximation of the extreme of the front by a finite population and are within the run-to-run range above. The results reported in Section 3 correspond, for each tariff, to the run with the median hypervolume.

3. Results and Discussion

3.1. Meteorological Forecasting Performance and Meta-Learner Weight Dynamics

The predictive reliability of the day-ahead HEMS fundamentally hinges upon the accuracy of the underlying meteorological forecasts, which directly drive both the rooftop PV generation estimates (P_{PV}) and the thermal load dynamics of the building envelope (P_{AC} and P_{CH}). The predictive performance of the evaluated deep architectures—LSTM [44], TCN [46], and TFT [47]—alongside the proposed multi-model stacking ensemble [48], was rigorously assessed on the hold-out test dataset across the entire 24 h horizon ($h+1$ to $h+24$). Table 5 and Table 6 compile the consolidated error metrics for ambient air temperature and global solar horizontal irradiance, respectively.

Table 5. Consolidated test-set predictive performance for ambient air temperature (°C) over the 24 h forecasting horizon.

Forecasting Model	MAE (°C)	RMSE (°C)	R^2	MAPE (%)
LSTM	0.9561	1.3115	0.8433	4.3150
TCN	1.0144	1.3965	0.8223	4.6079
TFT	0.9357	1.2934	0.8476	4.2286
Stacking Ensemble	**0.9270**	**1.2767**	**0.8515**	**4.2024**

Table 6. Consolidated test-set predictive performance for global solar radiation ($kW\,m^{-2}$) over the 24 h forecasting horizon.

Forecasting Model	MAE ($kW\,m^{-2}$)	RMSE ($kW\,m^{-2}$)	R^2	MAPE (%)
LSTM	0.0682	0.1223	0.8152	696.7887
TCN	0.0703	0.1275	0.7990	749.5103
TFT	0.0692	0.1227	0.8141	851.5613
Stacking Ensemble	**0.0673**	**0.1206**	**0.8203**	742.1276

As evidenced by the quantitative evaluation, the stacking ensemble provides the best performance in all four metrics for ambient temperature and in MAE, RMSE, and R^2 for solar radiation, whereas the LSTM attains the lowest full-horizon MAPE for solar radiation (696.79% against 742.13%). For ambient temperature, the ensemble attains the lowest mean absolute error (MAE = 0.9270 °C) and root mean square error (RMSE = 1.2767 °C), corresponding to error reductions of 3.04% and 2.65% over the standalone LSTM baseline, and 8.62% and 8.58% over the TCN. Furthermore, the coefficient of determination reaches

$R^2 = 0.8515$, confirming that the ensemble explains more than 85% of the total temperature variance. Among individual learners, the TFT demonstrates the highest standalone accuracy (MAE = 0.9357 °C), which is driven by its temporal multi-head self-attention mechanisms that effectively capture non-stationary daily cycles. For solar irradiance, the Stacking Ensemble achieves MAE = 0.0673 kW/m^2, RMSE = 0.1206 kW/m^2, and $R^2 = 0.8203$. The elevated MAPE values observed for solar radiation are an expected mathematical artefact stemming from near-zero denominator values during nocturnal and twilight intervals (Section 2), where an absolute error of a few W/m^2 divided by $|y| + \varepsilon$ yields a percentage error of several hundred percent; the full-horizon MAPE of radiation is therefore not used to rank the models.

Table 7 reports the radiation metrics restricted to daylight hours ($G \geq 0.05$ kW/m^2, 45.3% of the test observations) for the first lead time ($h + 1$), the horizon for which the test-set predictions were stored. Over these hours, the MAPE becomes meaningful (31–37%) and the stacking ensemble attains the lowest MAE, RMSE, MAPE, and WAPE and the highest R^2, which is followed closely by the TFT. The forecasting advantage of the ensemble is therefore metric-specific: it reduces the absolute and squared errors, which are the quantities that propagate into the PV and thermal models, while its full-horizon MAPE is dominated by twilight observations.

Table 7. Test-set predictive performance for global solar radiation at the first lead time ($h + 1$) restricted to daylight hours ($G \geq 0.05$ kW/m^2; 1765 observations).

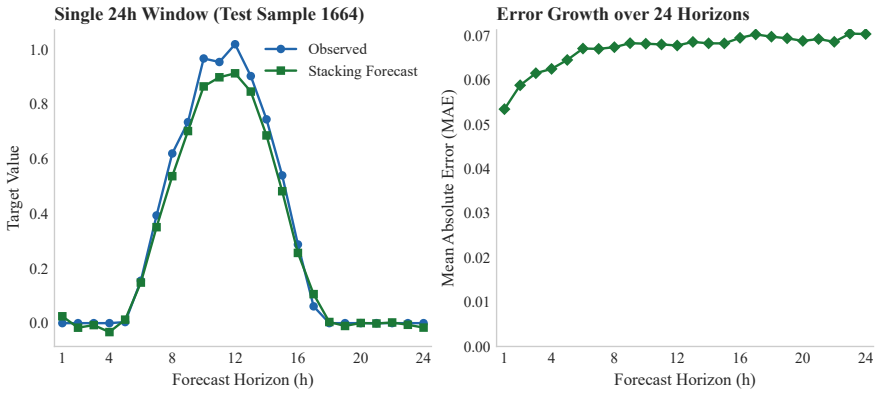
Model	MAE (kW/m^2)	RMSE (kW/m^2)	R^2	MAPE (%)	WAPE (%)
LSTM	0.1015	0.1360	0.7228	33.28	22.36
TCN	0.1096	0.1466	0.6781	37.34	24.15
TFT	0.0931	0.1271	0.7581	31.69	20.51
Stacking Ensemble	**0.0926**	**0.1266**	**0.7601**	**31.15**	**20.40**

Figure 7 visually validates the capacity of the models to track sharp diurnal transitions and peak thermal gradients across the 24 h horizon. A pivotal engineering advantage of the proposed stacking meta-learner is its transparent interpretability. Figure 8 illustrates the learned linear coefficients assigned to each base expert across all 24 lead times alongside their mean absolute weight contributions.

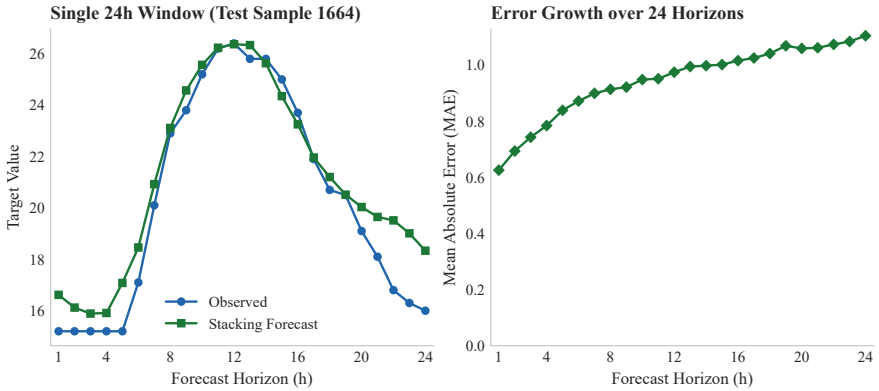
The weight trajectory analysis reveals that the meta-learner dynamically shifts authority among experts as a function of the lookahead horizon: short-term projections ($h + 1$ to $h + 4$) heavily leverage the high-frequency gating precision of the TFT, whereas longer lookahead intervals ($h + 12$ to $h + 24$) allocate increased weight to the recurrent gating of the LSTM and dilated causal convolutions of the TCN to maintain asymptotic stability. This horizon-adaptive blending suppresses the compounding drift error typical of single autoregressive models, establishing a robust foundation for day-ahead optimization.

3.2. 3D Multi-Objective Pareto Fronts and Operational Trade-Off Analysis

The tri-objective optimization problem formulated in Equation (50) was solved via NSGA-III across 200 generations with a population of 250 individuals. Figure 9 presents the resulting non-dominated three-dimensional Pareto frontiers in the objective space defined by user comfort index (U_c), daily SH operation cost (c_e), and daily CO_2 emissions (E_{CO_2}) under both the Brazilian White Tariff (TOU-1) and the Adapted Multi-Tier Tariff (TOU-2).



(**a**) Air Temperature



(**b**) Global Solar Radiation

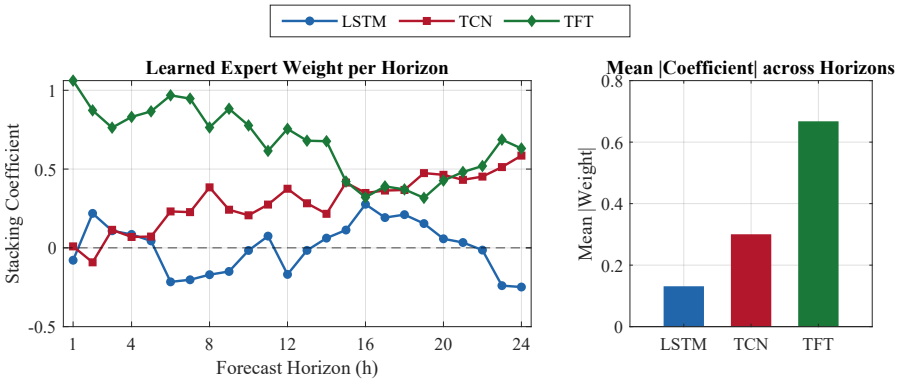
Figure 7. Multi-horizon 24-step-ahead test timelines comparing observed series against deep learning model predictions and cumulative multi-step error propagation for (**a**) ambient air temperature; (**b**) global solar radiation.

To quantify the operational boundaries and trade-off sensitivity, four representative solutions were identified on each frontier:

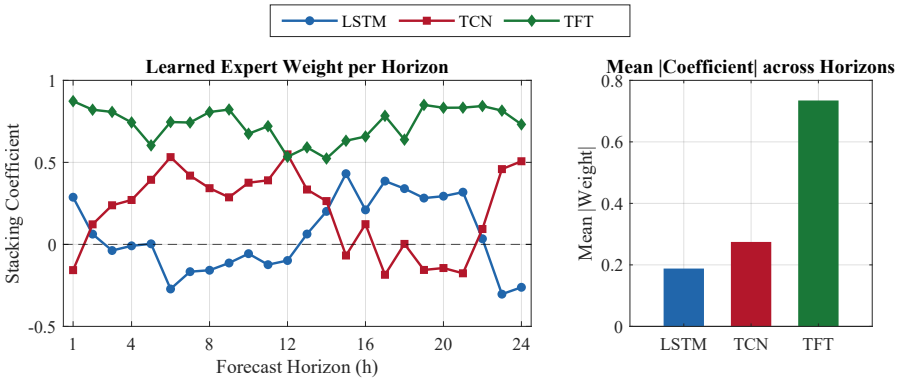
1. S_1 **(Minimum Cost Policy):** strictly minimizes net operational expenditure (c_e), aggressively curtailing load during high-tariff periods and shifting EV charging and shiftable appliances into solar surplus and off-peak hours.
2. S_2 **(Knee Point/Compromise Policy):** determined via maximum orthogonal Euclidean distance from the extreme boundary hyperplane in the normalized objective space. It delivers an optimal compromise between economic efficiency and occupant satisfaction.
3. S_3 **(Maximum Comfort Policy):** the solution of the front with the highest comfort index, i.e., the schedule closest to the highest historical usage probability intervals $f(i,j)$ found by the optimizer.
4. S_4 **(Minimum Emission Policy):** minimizes the total carbon footprint (E_{CO_2}) by restricting electricity imports during high-carbon grid generation windows and maximizing local PV self-consumption.

All four solutions are outputs of the optimization. In particular, S_3 is the maximum-comfort *optimized* schedule: it still benefits from the HEMS, because the EV charging follows the EVESS strategy and absorbs PV surplus. To assess the benefit of the HEMS against a household without management, a non-optimized reference S_0 was also simulated with the same weather, PV, and load data: each appliance starts at its most probable hours according to $f(i,j)$, as in the occupants' habitual routine, without any price or emission signal, and the EV is charged at P_{batmax} as soon as it is plugged in until SOC_{max} is reached (uncontrolled

charging). S_0 is evaluated with the same objective functions, Equations (43), (44), and (49), and its results are included in Table 8. By construction, its comfort index equals the theoretical maximum $U_c^{max} = 1.1982$ of Equation (45).



(**a**) Air Temperature



(**b**) Global Solar Radiation

Figure 8. Meta-learner weight dynamics across the 24 h forecast horizon: learned linear regression coefficients (left) and mean absolute weight allocation across all lead times (right) for (**a**) ambient air temperature; (**b**) global solar radiation.

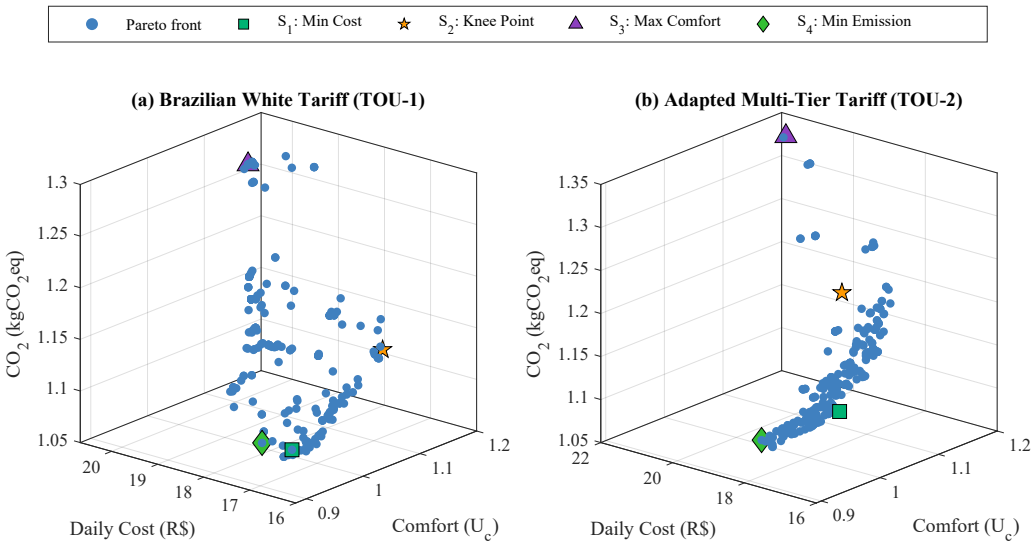


Figure 9. Non-dominated three-dimensional Pareto frontiers computed by NSGA-III illustrating the multi-way operational trade-offs among U_c, operation costs (BRL), and CO_2 emissions ($kgCO_2eq$) under: (**a**) Brazilian White Tariff (TOU-1); (**b**) Adapted Multi-Tier Tariff (TOU-2), highlighting the representative boundary solutions (S_1, S_3, S_4) and the compromise knee point (S_2).

All four solutions are outputs of the optimization. In particular, S_3 is the maximum-comfort *optimized* schedule: it still benefits from the HEMS, because the EV charging follows the EVESS strategy and absorbs PV surplus. To assess the benefit of the HEMS against a household without management, a non-optimized reference S_0 was also simulated with the same weather, PV, and load data: each appliance starts at its most probable hours according to $f(i, j)$, as in the occupants' habitual routine, without any price or emission signal, and the EV is charged at P_{batmax} as soon as it is plugged in until SOC_{max} is reached (uncontrolled charging). S_0 is evaluated with the same objective functions, Equations (43), (44), and (49), and its results are included in Table 8. By construction, its comfort index equals the theoretical maximum $U_c^{max} = 1.1982$ of Equation (45).

The NSGA-III was run ten times per tariff with independent seeds (Section 2.8); the results below correspond to the run with the median hypervolume. In all runs, the whole final population (250 solutions) was non-dominated.

Table 8 summarizes the consolidated performance metrics for all four representative solutions across both tariff structures.

Under the Brazilian White Tariff (TOU-1), the non-optimized reference S_0 costs BRL 22.74/day and emits 1.600 kgCO_2eq/day with the maximum comfort index $U_c^{max} = 1.1982$ by construction. The knee point S_2 costs BRL 16.57/day, i.e., 27.13% less than S_0 (BRL 185.04/month), keeps 90.2% of the theoretical maximum comfort ($U_c = 1.0806$), and emits 28.26% less. The minimum-cost solution S_1 reduces the cost by 29.27% with respect to S_0 but with a 26.43% lower comfort index. Within the optimized front, moving from the maximum-comfort schedule S_3 ($U_c = 1.1770$, 98.2% of U_c^{max}) to S_1 saves BRL 4.60/day (22.23%, or BRL 137.90/month) at the expense of a 25.11% reduction of the comfort index, whereas S_2 retains 91.81% of the comfort of S_3 at a cost 19.87% lower (BRL 123.29/month). Relative to S_1, S_2 requires only BRL 0.49/day of additional cost (+3.03%) for a 22.59% higher comfort index. The saving with respect to S_0 comes mainly from two changes (Table 9): the EV, whose uncontrolled charging in S_0 starts at 8 kW as soon as it is plugged in and imports up to 5.1 kW from the grid in interval 12, and is charged in S_2 with the PV surplus of intervals 12–17; and the evening showers of S_0, two of which fall in the peak block, are moved to midday. The operating intervals of every appliance and of the EV charging in S_0, S_2, and S_3 are given in Table 9.

Table 8. Consolidated performance metrics of representative 3-objective Pareto solutions under Brazilian White Tariff (TOU-1) and Adapted Multi-Tier Tariff (TOU-2) (run with the median hypervolume among ten).

Performance Metric	Brazilian White Tariff (TOU-1)				Adapted Multi-Tier Tariff (TOU-2)			
	Min C (S_1)	**Knee (S_2)**	**Max U (S_3)**	**Min E (S_4)**	**Min C (S_1)**	**Knee (S_2)**	**Max U (S_3)**	**Min E (S_4)**
Daily Cost (BRL/day)	16.08	16.57	20.68	17.06	16.93	19.50	21.48	17.90
Comfort Index U_c	0.8815	1.0806	1.1770	0.9081	0.9882	1.1495	1.1755	0.9146
CO_2 Emissions (kg)	1.1005	1.1479	1.2547	1.0891	1.1192	1.1836	1.3351	1.0946
Monthly Cost (BRL/month)	482.46	497.07	620.36	511.81	507.88	584.93	644.47	537.00
Non-optimized reference S_0 and variation of the HEMS solutions relative to S_0								
	TOU-1			**TOU-2**				
	S_0	**S_1 vs. S_0**	**S_2 vs. S_0**	**S_0**	**S_1 vs. S_0**	**S_2 vs. S_0**		
Daily Cost (BRL/day)	22.74	−29.27%	−27.13%	24.46	−30.77%	−20.27%		
Comfort Index U_c	1.1982	−26.43%	−9.82%	1.1982	−17.52%	−4.06%		
CO_2 Emissions (kg)	1.6001	−31.22%	−28.26%	1.6001	−30.05%	−26.03%		
Max. Grid Import in Peak Block (kW)	1.67	0.53	0.54	1.51	0.16	1.20		
PV Self-Consumption (%)	50.7	97.5	94.0	50.7	98.2	93.8		

Table 9. Hourly intervals (local hour $[i-1, i)$) in which each appliance operates in the non-optimized reference (S_0), knee-point (S_2), and maximum-comfort (S_3) schedules under TOU-1, and EV charging (intervals, mean charger power, and energy).

Appliance ($n \times c_d$)	S_0 (Non-Optimized)	S_2 (Knee Point)	S_3 (Max. Comfort)
AC Bedroom (1 × 6 h)	23–24, 1–4	23–24, 1–4	24, 1–5
AC Suite (1 × 8 h)	22–24, 1–5	22–24, 1–5	22–24, 1–5
Washing Machine (1 × 1 h)	10	10	10
Electric Oven (1 × 1 h)	13	13	13
Dishwasher (1 × 1 h)	10	10	10
Electric Iron (1 × 1 h)	16	9	16
Clothes Dryer (1 × 1 h)	10	9	9
Ceiling Fan (1 × 6 h)	22–24, 1–3	5–10	1–6
Floor Fan (1 × 6 h)	23–24, 1–4	2–7	1–6
Electric Shower (5 × 1 h, 15 min each)	8, 19, 20, 21, 22	8, 11, 13, 14, 15	8, 9, 19, 20, 21
EV Charging: Intervals	12–13	12–17, 22	12–18
EV Charging: Mean Power; Energy	5.86 kW; 11.7 kWh	1.67 kW; 11.7 kWh	1.67 kW; 11.7 kWh

Under the Adapted Multi-Tier Tariff (TOU-2), S_0 costs BRL 24.46/day, because the more segmented tariff places part of the habitual consumption in peak blocks. The minimum-cost policy (S_1) achieves BRL 16.93/day ($U_c = 0.9882$), while the knee-point solution (S_2) costs BRL 19.50/day with $U_c = 1.1495$, preserving 97.79% of the comfort of S_3 (95.9% of U_c^{max}) at a cost 20.27% lower than that of S_0. The minimum-emission policy (S_4) reduces daily emissions to 1.0891 kgCO_2eq under TOU-1 and 1.0946 kgCO_2eq under TOU-2, corresponding to reductions of 13.20% and 18.01%, respectively, relative to S_3, and of about 32% relative to S_0. Because the hourly emission factor varies by only about ±11% over the day (Section 2.8), most of this reduction comes from the PV self-consumption enabled by the EV charging, which also reduces cost: S_4 emits only 1.0% (TOU-1) and 2.2% (TOU-2) less than S_1.

3.3. Two-Dimensional Pairwise Trade-Off Projections and Frontier Geometry

To inspect the underlying geometric curvature and cross-objective coupling, Figure 10 depicts the two-dimensional pairwise projections of the 3D non-dominated front under TOU-1.

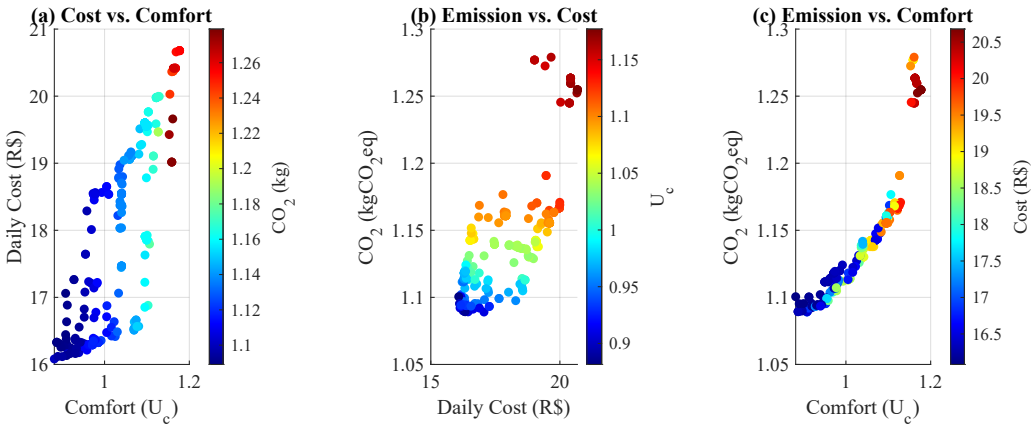


Figure 10. Two-dimensional pairwise projections of the tri-objective Pareto front for the Brazilian White Tariff (TOU-1): (**a**) daily cost vs. occupant comfort index; (**b**) CO_2 emissions vs. daily cost; (**c**) CO_2 emissions vs. occupant comfort index, where marker color denotes the third objective.

The cost vs. comfort projection (Figure 10a) shows a convex trade-off: from S_1 to S_2, the comfort index increases by 22.6% for a 3.0% increase in cost, whereas from S_2 to S_3, a further 8.9% increase in comfort costs 24.8% more, because the remaining comfort gains

require operating the showers and part of the EV charging in the late afternoon and evening, when PV generation is no longer available and the tariff is higher (peak block 17:00–20:00, BRL 1.42/kWh). Figure 10b,c illustrate the environmental trade-off: emissions and cost are strongly correlated along the front, because both are reduced by supplying the loads and the EV with the midday PV surplus; the residual conflict arises in the evening, when the emission factor is lowest but the tariff is highest, so that purely economic optimization does not guarantee minimum emissions, although the difference between S_1 and S_4 is small.

3.4. Load-Class Segregated Appliance Scheduling and Preference Alignment

Figure 11 displays the 24 h operation schedule for all ten controllable household appliances under the knee-point solution (S_2) for TOU-1, which is juxtaposed with their underlying comfort probability profiles $f_{i,j}$.

The scheduling patterns reveal a fundamental divergence in operational mechanisms across load categories:

- **Shiftable Deferrable Loads (WM, CD, DW, EO, EI):** The clothes dryer and the electric iron operate in interval 9 (08:00–09:00) and the washing machine and the dishwasher in interval 10, at the morning usage peak of these appliances and as PV generation rises; the electric oven operates in interval 13, which is at its highest usage probability and close to the PV maximum. None of the shiftable appliances operates in the peak tariff block.
- **Thermostatically Controlled and Continuous Loads (AB, AS, CF, FF, ES):** Bedroom (AB) and suite (AS) air conditioners operate during the night-time sleeping intervals (22:00–04:00 and 21:00–05:00, respectively), exploiting low off-peak tariff rates (BRL 0.67/kWh) and reduced ambient heat transfer. The electric shower (ES) keeps the morning shower (interval 8) but moves the other four showers to intervals 11 and 13–15, when they are supplied by PV and the inlet water is warmest (3.4–4.2 kW instead of up to 5.0 kW at night), at the cost of a lower comfort term for this appliance. The fans, whose energy is small (0.45 kWh/day each), are moved to the early morning.

In Figure 11, each bar is the mean electrical power drawn by the appliance in the scheduled interval: the nominal power multiplied by p_{cd} for the constant-power appliances, and the power given by the thermal models for the air conditioners and the shower. Every appliance has a single daily cycle except the shower (five cycles); the start interval of every cycle is listed in Table 9.

3.5. Physics-Coupled Dynamic Thermal Response of Building and TCLs

Figure 12 details the thermodynamic and electrical interactions of the two thermostatically controlled loads: the dual-zone air-conditioning system and the tankless electric water heater.

In Figure 12a, the 4R3C thermal network tracks the indoor temperature of the suite, whose unit operates from 21:00 to 05:00 (intervals 22–24 and 1–5). After switch-off, T_a follows the outdoor temperature with a delay of about two hours and stays above it in the late afternoon, when the outdoor temperature falls after its maximum of 27.0 °C in interval 14 (13:00–14:00). When the unit is switched on, it first draws about 1.0 kW to bring T_a back to T_{set}; once T_{set} is reached, the power is only that needed to compensate the heat gains, 0.2–0.3 kW, which depend on the difference between the outdoor and indoor temperatures. All curves in Figure 12 are the direct outputs of the models of Sections 2.5.1 and 2.5.2. In Figure 12b, the electrical power of the tankless heater, Equations (19)–(21), varies between 5.01 kW at night ($T_{in} \approx 17.7$ °C) and 3.37 kW in interval 14 ($T_{in} = 25.0$ °C); with 15-min showers, the energy of each shower ranges from 0.84 to 1.25 kWh. Table 10 compares the daily energy of the electric shower obtained with the thermodynamic model and with

a fixed rated power of 5.5 kW, as assumed in conventional HEMS models, for the same five showers of S_2 and the same weather. The fixed-power model overestimates the daily energy by 42.2% (2.05 kWh/day) or 29.7% when the difference is expressed relative to the fixed-power estimate. The 28.5% reported in the original version was obtained with an implementation that did not apply the shower duration and is replaced by these values.

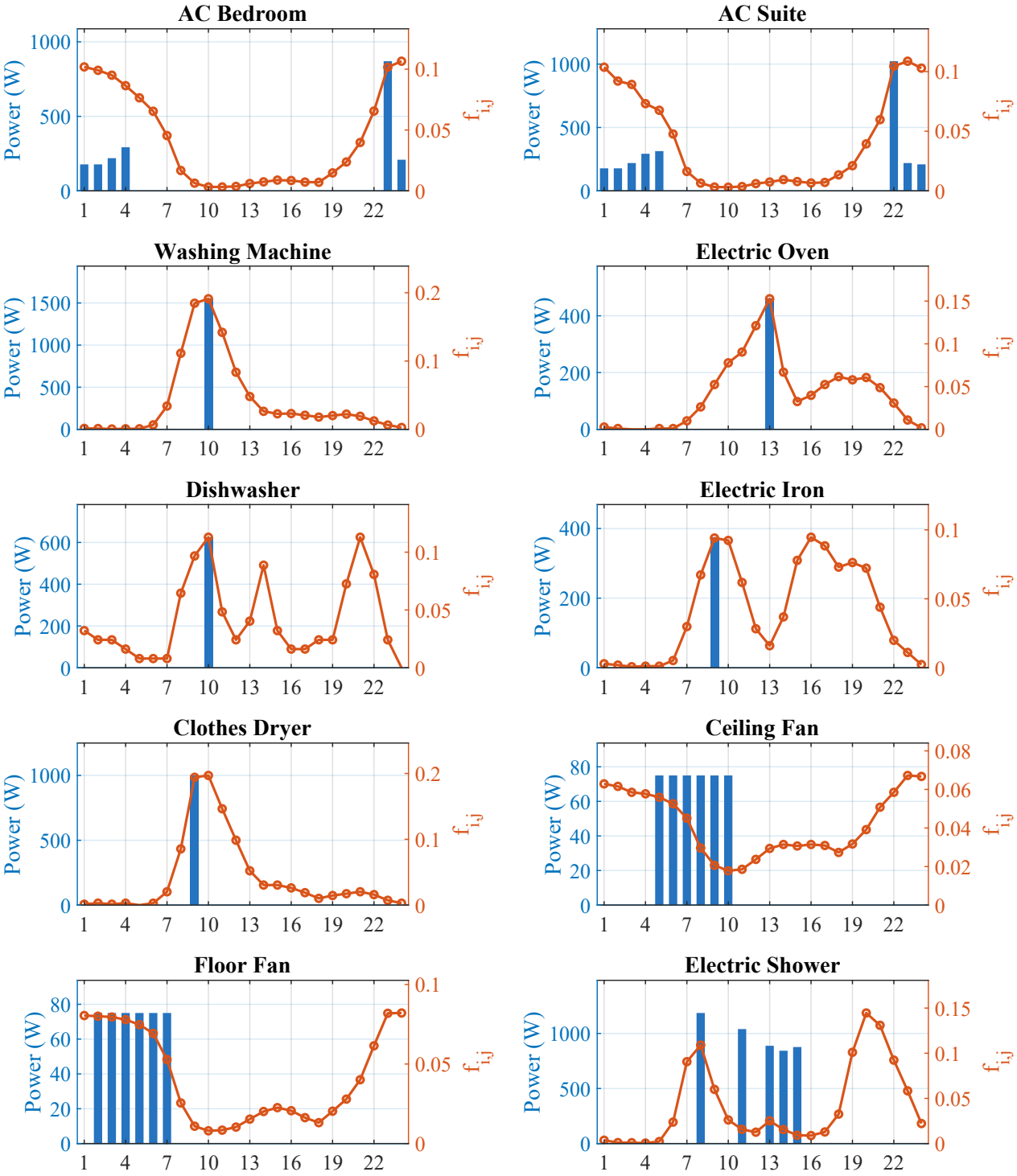


Figure 11. Optimal dispatch schedules of all ten controllable household appliances under the knee-point policy (S_2) for the Brazilian White Tariff (TOU-1), displaying operating power (**left axis**) and empirical usage probability $f_{i,j}$ (**right axis**).

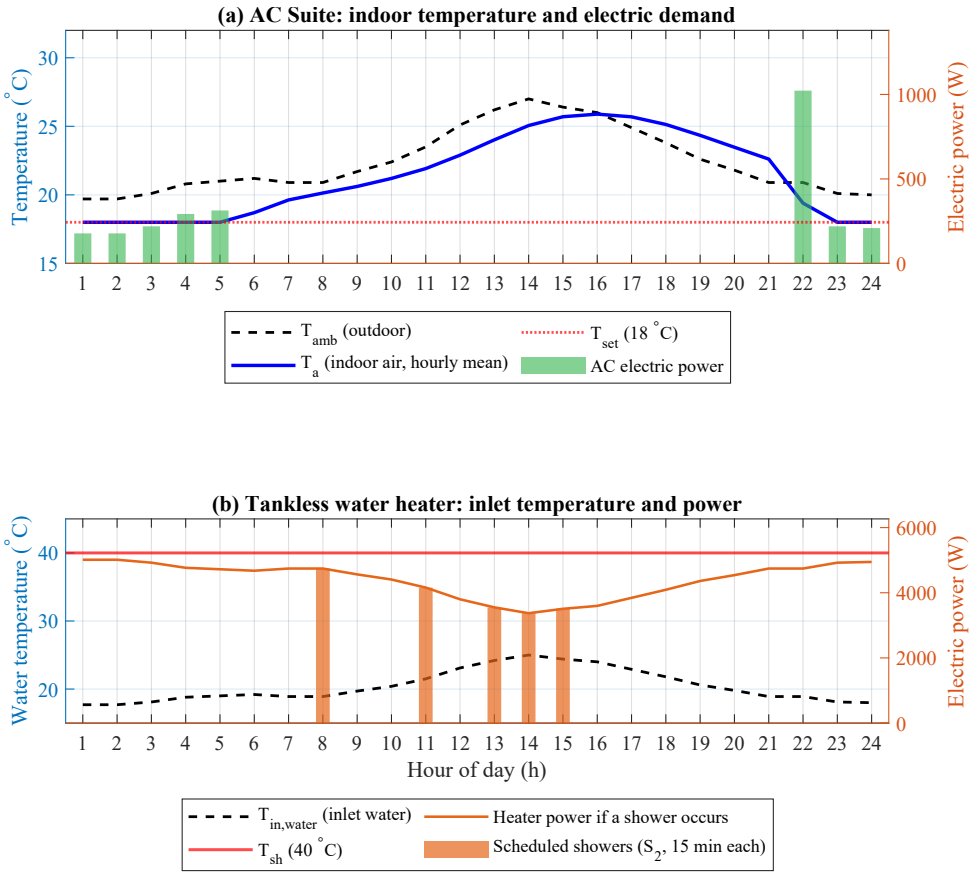


Figure 12. Thermodynamic and electrical dynamics of thermostatically controlled loads (TCLs) in the knee-point schedule S_2 (TOU-1): (**a**) suite air conditioner: indoor air temperature (T_a, hourly mean), ambient temperature (T_{amb}), comfort setpoint ($T_{\text{set}} = 18\,^{\circ}\text{C}$), and electrical power demand (P_{ar}); (**b**) electric water heater inlet water temperature ($T_{\text{in,water}}$), comfort target ($T_{sh} = 40\,^{\circ}\text{C}$), electric power of the heater if a shower occurs in each hour (P_s), and the five scheduled showers.

Table 10. Daily electricity consumption of the electric shower with the fixed-power and thermodynamic models for the same schedule (S_2, TOU-1) and weather.

Quantity	Fixed Power (5.5 kW)	Thermodynamic Model
Power in each cycle (kW)	5.50	3.37–4.74
Active time per cycle (h)	0.25	0.25
Daily energy, 5 cycles (kWh/day)	6.88	4.83
Difference, $(E_{fix} - E_{th})/E_{fix}$	29.7%	
Difference, $(E_{fix} - E_{th})/E_{th}$	42.2%	

3.6. Smart Home Net Power Balancing and PV Self-Consumption Under Law 14300/2022

Figure 13 illustrates the aggregate daily power profiles of the smart home under the knee-point schedule, displaying total residential demand P_{SH}, on-site solar generation P_{PV}, net demand $P_{\text{net}} = P_{\text{SH}} - P_{\text{PV}}$, and baseline non-controllable loads P_{NC}.

During maximum solar irradiance (10:00–15:00), rooftop PV generation peaks at 3.08 kW in interval 12 (11:00–12:00), with 18.9 kWh in the day, completely covering concurrent household consumption and generating an uncurtailed solar surplus. Under Brazilian Law 14300/2022, grid injection credits are subject to increasing wire distribution tariff charges (the "Fio B" component), rendering direct on-site self-consumption significantly more profitable than grid injection. The proposed HEMS maximizes self-consumption by actively co-scheduling shiftable appliances and EV charging during the peak solar window, increasing the on-site PV self-consumption ratio from 50.7% in the non-optimized reference

S_0, in which 9.3 kWh are exported, to 94.0% in S_2, in which only 1.1 kWh is exported (in interval 11, while the EV is still away).

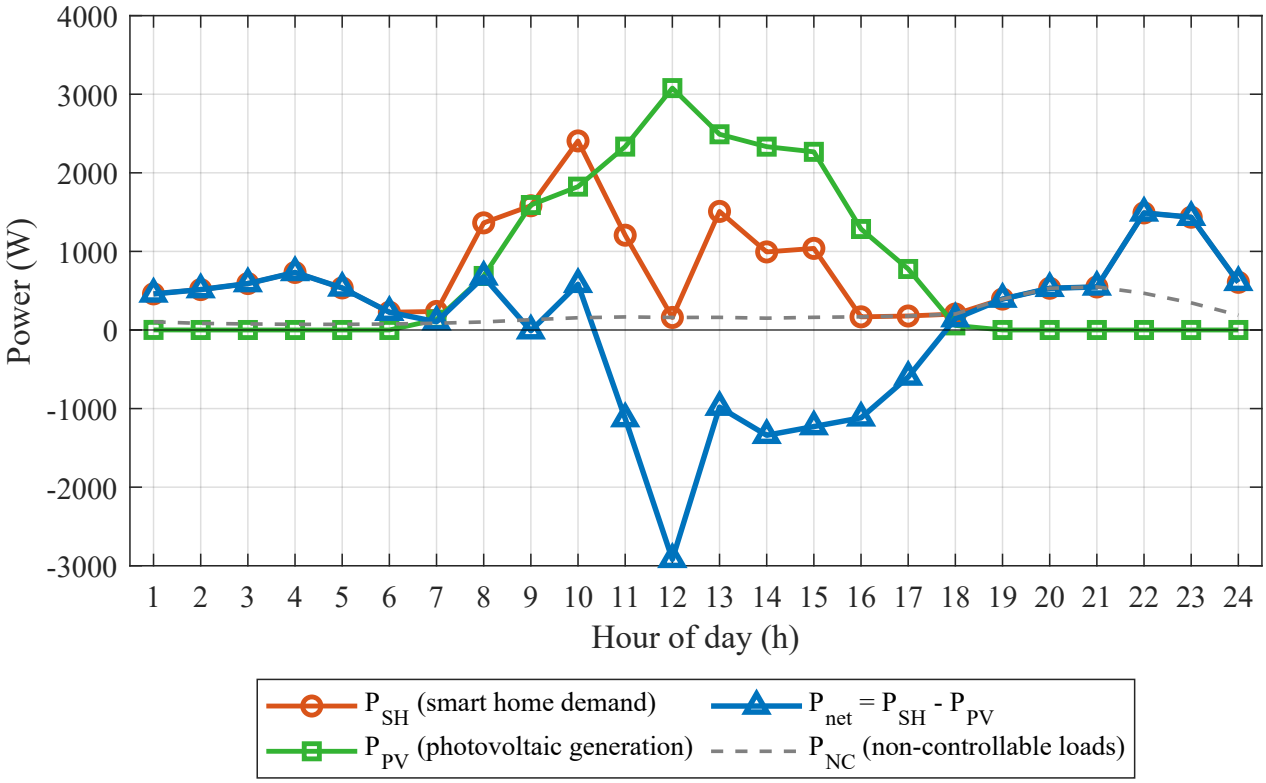


Figure 13. Consolidated daily power profiles of total smart home demand (P_{SH}), rooftop photovoltaic generation (P_{PV}), net demand (P_{net}), and non-controllable baseload (P_{NC}) under the optimal knee-point schedule for TOU-1.

3.7. EV Battery Storage Dynamic Dispatch and Peak-Shaving Arbitrage

Figure 14 illustrates the coordinated dispatch of the electric vehicle battery energy storage system (EVESS) and the resulting interaction with the distribution network.

As shown in Figure 14a, during the travel period (06:00–11:00), the battery SOC decreases from 95% to 66.3%, respecting the mobility safety buffer ($SOC \geq 40\%$). When the EV returns, it is charged between 11:00 and 17:00 (intervals 12–17) only with the PV surplus, reaching 86.3%, and the remaining 8.6 points are charged at 3.5 kW in interval 22 (21:00–22:00), in the off-peak block, so that the SOC returns to its initial value of 95%. Figure 14b shows that the grid import P_{grid} stays between 0.15 and 0.54 kW during the peak block, thereby reducing the household's exposure to higher electricity prices (BRL 1.42/kWh). The EV is not discharged to supply this load (the charger is unidirectional, Section 2.7); the low import results from not charging the EV and from not scheduling shiftable and thermal loads in the peak block.

3.8. Cross-Solution Grid Interaction Dynamics and Distribution Feeder Impact

Figure 15 compares the grid power exchange profiles P_{grid} across all four representative Pareto solutions (S_1, S_2, S_3, S_4) and the non-optimized reference S_0.

The comparative analysis reveals distinct grid interaction characteristics:

- The minimum cost policy (S_1) keeps the imports in the peak block between 0.16 and 0.53 kW and absorbs the whole PV surplus, but it concentrates the EV top-up charging and the start of the air conditioners in interval 22, when the import reaches 4.65 kW.

- The maximum comfort policy (S_3) produces a evening grid import of 1.44–1.67 kW in the peak block (intervals 18–20) and 1.73 kW in interval 21 due to the evening showers scheduled at their most probable hours.
- The knee point policy (S_2) holds the imports in the peak block between 0.15 and 0.54 kW, which is a reduction of 67.4% of the maximum peak-block import with respect to both S_3 and S_0 (1.67 kW). This reduction is restricted to the tariff peak: the EV top-up charging (3.5 kW) and the start of the air conditioners coincide in interval 22 (21:00–22:00, off-peak), when S_2 imports 4.99 kW, so the daily maximum import is not reduced with respect to S_0 (5.08 kW, caused by the uncontrolled EV charging in interval 12) and is higher than that of S_3 (1.73 kW).
- The minimum emission policy (S_4) yields the lowest carbon footprint (1.0891 $kgCO_2eq$); its imports in the peak block (0.17–1.05 kW) are higher than those of S_2, because the emission factor is lowest in intervals 19–21, whereas its import in interval 22 (3.19 kW) is lower.

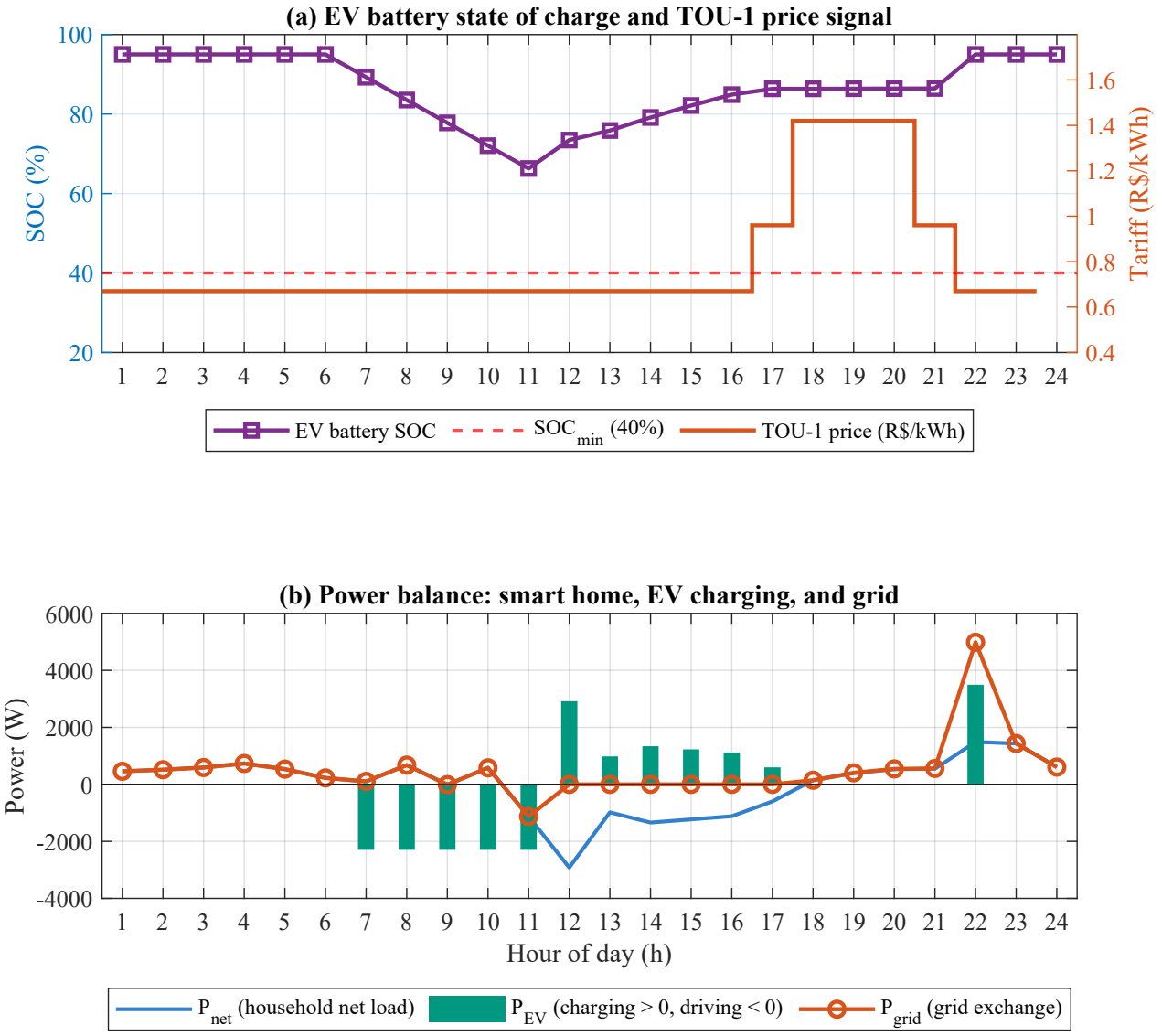


Figure 14. Electric vehicle battery storage (EVESS) dispatch and grid power exchange: (**a**) battery state of charge (SOC) evolution and time-of-use tariff rate with the safety buffer (SOC_{min} = 40%); (**b**) power flow balance among household net load (P_{net}), net EV battery power (P_{EV}), obtained as the difference between charger power (P_{bat}) and EV driving power (P_{ope}), and grid power exchange (P_{grid}).

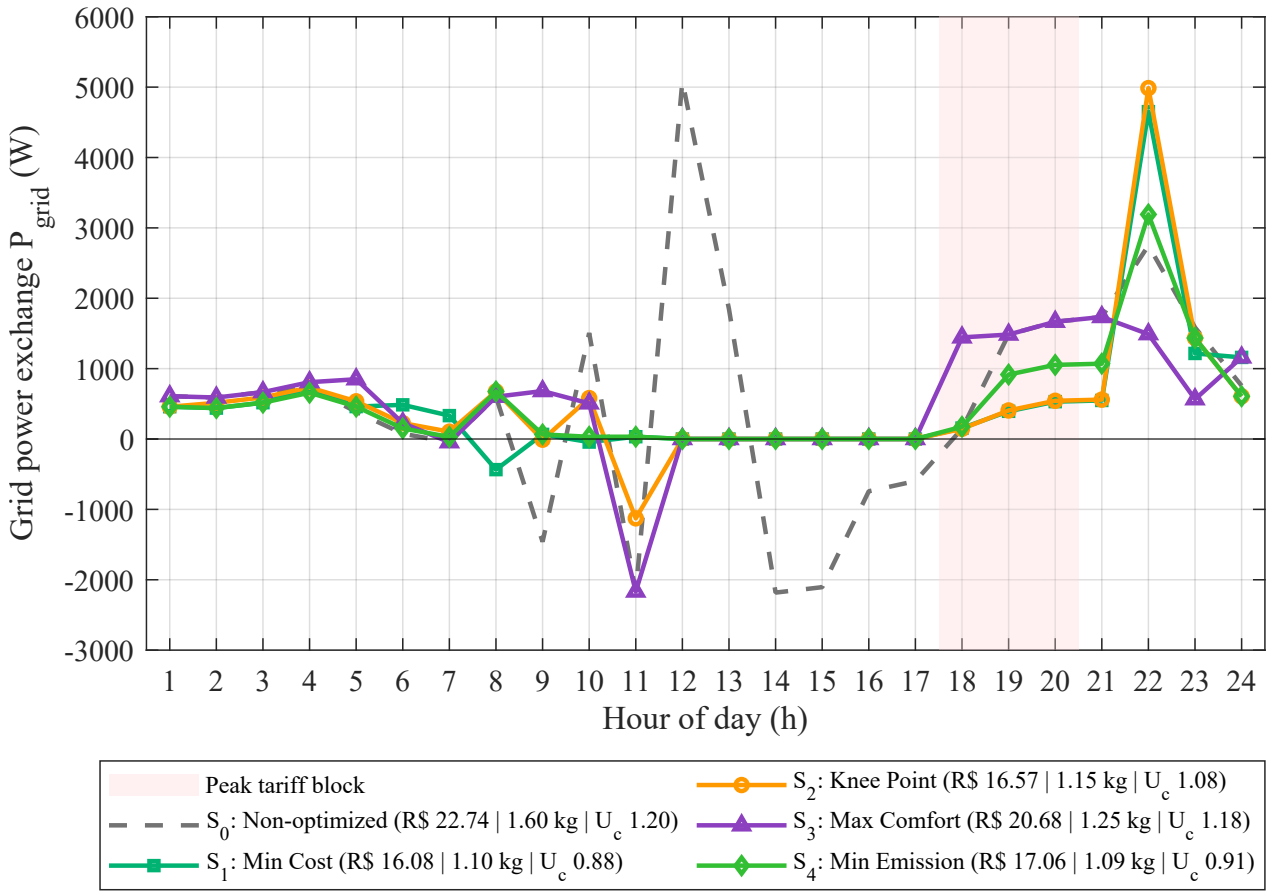


Figure 15. Comparison of grid power exchange profiles (P_{grid}) across representative Pareto solutions: S_1 (Min Cost), S_2 (Knee Point), S_3 (Max Comfort), and S_4 (Min Emission), and the non-optimized reference S_0, under the Brazilian White Tariff (TOU-1); the shaded area is the peak tariff block.

3.9. Consolidated 24-Hour Subsystem Operating Profile for the Knee Point Policy

Figure 16 presents a synchronized breakdown of all four core energy subsystems under the knee point policy (S_2): (1) net household demand without EV, (2) grid power exchange P_{grid}, (3) EV battery power P_{car}, and (4) EV battery state of charge SOC_{car}.

The synchronized profiles demonstrate multi-energy coordination: the midday PV surplus is absorbed by EV charging, while the remaining EV charging is postponed to the off-peak interval 22, after the peak block, resulting in a low grid exchange during the peak tariff block; the highest import of the day occurs in interval 22 when the EV top-up charging and the start of the air conditioners coincide.

3.10. Consolidated Metric Evaluation Across Representative Solutions

Finally, Figure 17 provides a direct bar-chart comparison of the three objective metrics (user comfort index, daily electricity cost, and daily CO_2 emissions) across the four representative Pareto solutions (S_1, S_2, S_3, S_4).

The quantitative comparison shows the balance provided by the knee point solution (S_2): it achieves $U_c = 1.0806$ (91.8% of the 1.1770 maximum of S_3), a daily cost of BRL 16.57 (close to the BRL 16.08 minimum of S_1 and 27.1% below the non-optimized reference S_0), and emissions of 1.1479 kgCO_2eq (5.4% above the minimum of S_4), which makes it a balanced benchmark for automated residential energy management.

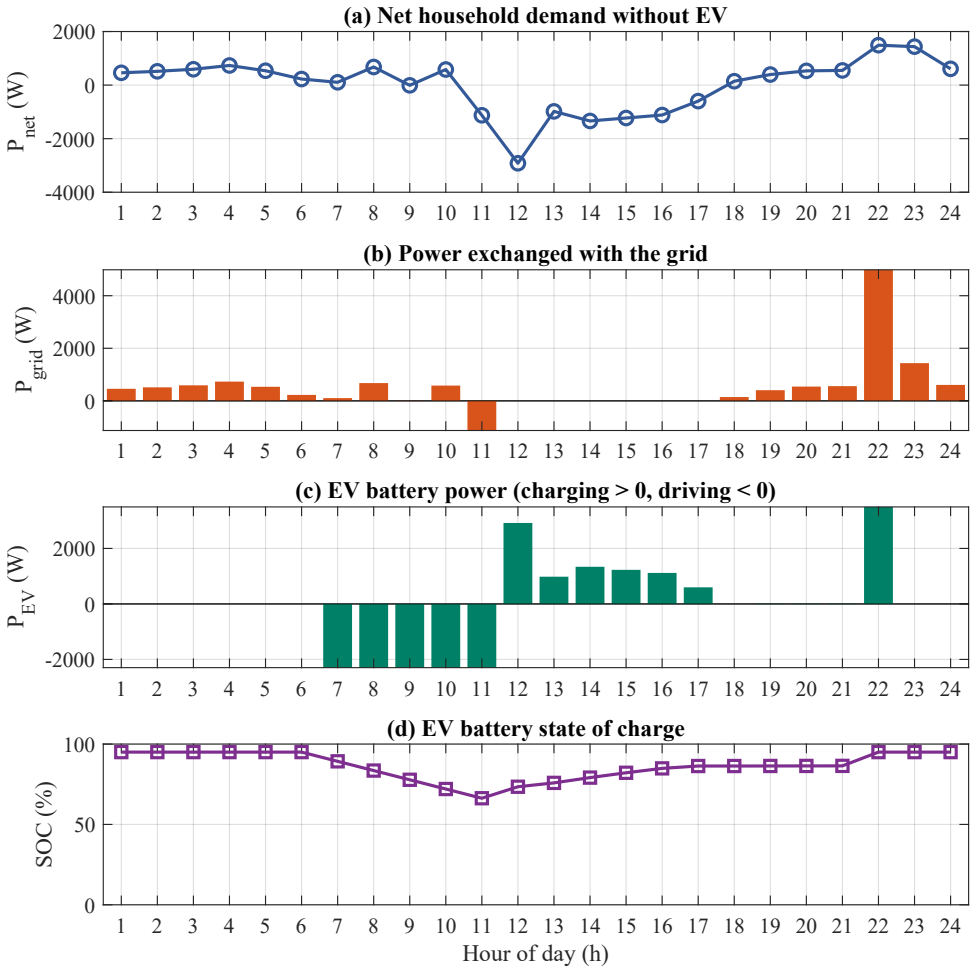


Figure 16. Synchronized 24 h subsystem operating profiles for the multi-objective knee-point compromise solution (S_2) under TOU-1: (1) net household demand without EV; (2) grid power exchange (P_{grid}); (3) EV battery power (P_{car}); (4) EV battery state of charge (SOC_{car}).

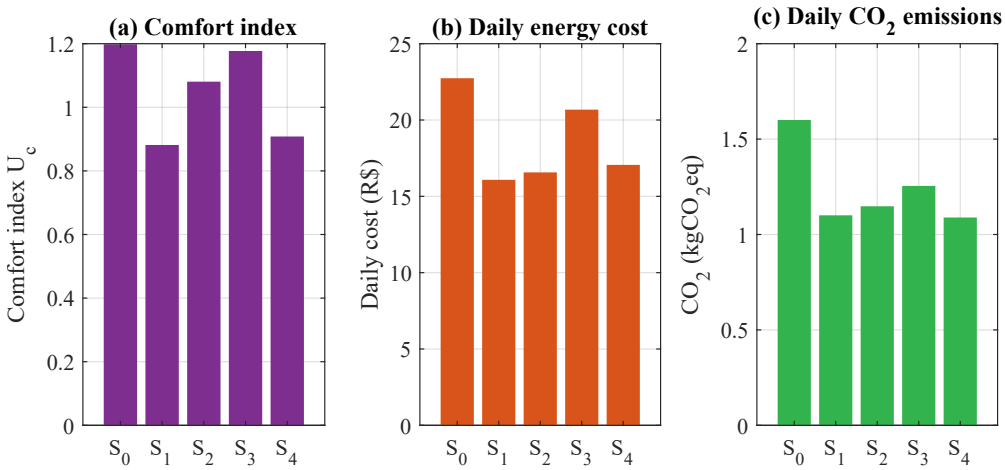


Figure 17. Multi-objective performance comparison across representative Pareto solutions (S_1: Min Cost, S_2: Knee Point, S_3: Max Comfort, S_4: Min Emission) and the non-optimized reference (S_0) under the Brazilian White Tariff (TOU-1): (**a**) user comfort index (U_c); (**b**) daily energy cost (BRL); (**c**) daily CO_2 emissions ($kgCO_2eq$).

3.11. Comparison Between NSGA-III and NSGA-II

To verify the choice of NSGA-III, the problem of Equation (50) was also solved with NSGA-II [42] under identical conditions: the same chromosome, constraints, weather and tariff data (TOU-1), the same population size (250), number of generations (200) and

crossover and mutation operators, and therefore the same budget of about 50,000 fitness evaluations; only the selection of the next generation differs (reference points in NSGA-III, crowding distance in NSGA-II). Both algorithms were run ten times with the same seeds. The fronts were compared using the hypervolume (HV) of the front normalized by the ideal and nadir points of the union of all fronts, with reference point $(1.1, 1.1, 1.1)$ [54], which measures convergence and diversity jointly; the spacing metric, which measures the uniformity of the distribution; the number of non-dominated solutions; the best value reached in each objective; the generation at which the HV reaches 99% of its final value; and the computational time. Table 11 summarizes the results (mean $\pm$ standard deviation over the runs).

The two algorithms exhibited comparable performance in terms of individual objective extremes, but NSGA-III achieved a higher mean normalized hypervolume (1.193 ± 0.038) than NSGA-II (1.115 ± 0.029), indicating better overall convergence and coverage of the three-objective Pareto front. NSGA-III also reached 99% of its final hypervolume earlier, at generation 139 ± 33, compared with 177 ± 12 for NSGA-II, although its results showed greater variability across runs. Regarding the extreme objective values, NSGA-III achieved slightly lower mean minimum cost and minimum emissions, whereas NSGA-II obtained a higher and less variable maximum comfort index. The spacing indicator was also slightly better for NSGA-II, suggesting a more uniform distribution of solutions according to this metric. In terms of computational effort, NSGA-II was approximately five times faster, requiring 5.4 ± 0.3 min per run, compared with 29.3 ± 8.9 min for NSGA-III. This overhead is nevertheless acceptable for the proposed day-ahead scheduling framework, in which optimization is performed before real-time operation. Overall, these results support the use of NSGA-III when improved Pareto-front quality is prioritized, while NSGA-II remains a computationally feasible alternative when computational efficiency is the primary concern.

Table 11. NSGA-III versus NSGA-II under the same computational budget (TOU-1, ten runs, mean $\pm$ standard deviation).

Indicator	NSGA-III	NSGA-II
Normalized hypervolume (higher is better)	1.193 ± 0.038	1.115 ± 0.029
Spacing (lower is better)	0.0202 ± 0.0034	0.0183 ± 0.0024
Non-dominated solutions in the final population	250.0 ± 0.0	249.2 ± 2.5
Minimum c_e (BRL/day)	16.21 ± 0.09	16.27 ± 0.09
Maximum U_c	1.170 ± 0.025	1.186 ± 0.006
Minimum E_{CO_2} ($kgCO_2eq$/day)	1.093 ± 0.007	1.095 ± 0.007
Generation at which HV reaches 99% of its final value	139 ± 33	177 ± 12
Computational time per run (s)	29.3 ± 8.9	5.4 ± 0.3

3.12. Sensitivity Analysis

The robustness of the results was assessed by perturbing one group of inputs at a time (TOU-1) in two ways: (i) *ex post*, by re-evaluating the nominal schedules of S_1 and S_2 with the perturbed inputs, without re-optimizing, which isolates the effect of the input on cost and emissions; and (ii) *re-optimized*, by running NSGA-III again with the perturbed inputs (five seeds) and comparing the median of the representative solutions with the median of the nominal runs with the same seeds. The following scenarios were considered, and the corresponding results are presented in Table 12:

- **Tariff level:** all consumption and injection prices multiplied by 0.8 and 1.2, keeping the block structure.
- **Forecast errors:** the day-ahead temperature and irradiance series shifted by $\pm$ the test-set RMSE of the stacking ensemble (temperature ± 1.28 °C; irradiance ± 0.12 kW/m^2

in daylight hours, limited to $G \geq 0$), which bounds the typical forecast error of Section 3.1.

- **Thermal parameters:** all envelope resistances and capacitances multiplied by 0.8 and 1.2.
- **Solar gains:** inclusion of the solar terms described in Section 2.5.1, with a window area $A_w = 1.2$ m^2 (consistent with R_w for 4-mm glazing), SHGC $= 0.85$, outer-wall absorptance $\alpha = 0.5$, and $A_m = 10$ m^2; the global horizontal irradiance is used as an upper bound of the irradiance on the façade.
- **Variable COP:** COP increasing linearly as the outdoor temperature decreases, $COP(T_{amb}) = COP_{rated}\,[1 + 0.25\,(35 - T_{amb})/15]$, i.e., a 25% variation between 35 and 20 °C instead of the constant rated value.

Table 12. Sensitivity of the knee point (S_2) and minimum-cost (S_1) solutions to the main inputs (TOU-1). Values are relative changes (%) with respect to the nominal case. Ex post: nominal schedules re-evaluated with the perturbed inputs; re-optimized: median of five runs with the perturbed inputs against the median of the nominal runs with the same seeds.

	S_2 (Knee Point)			S_1 (Min. Cost)		
Scenario	Δc_e	ΔU_c	ΔE_{CO_2}	Δc_e	ΔU_c	ΔE_{CO_2}
Ex post (schedules fixed)						
Temperature − RMSE	−8.1	0.0	−9.3	−8.3	0.0	−9.9
Temperature + RMSE	+7.8	0.0	+9.0	+8.1	0.0	+9.7
Irradiance − RMSE	+15.4	0.0	+15.5	+15.7	0.0	+15.7
Irradiance + RMSE	−21.1	0.0	−19.7	−21.1	0.0	−19.4
With solar gains	+0.2	0.0	+0.2	+0.2	0.0	+0.2
Variable COP	−3.6	0.0	−4.1	−3.7	0.0	−4.3
Re-optimized						
Tariff × 0.8	−14.0	−2.3	−2.0	−10.5	−3.2	+0.5
Tariff × 1.2	+10.8	−2.1	−2.0	+11.6	−7.1	+0.1
Temperature − RMSE	−8.0	−2.1	−11.7	−8.0	+6.1	−9.3
Temperature + RMSE	−0.5	−1.4	+7.4	+9.0	+0.5	+11.1
Irradiance − RMSE	+13.4	+2.8	+15.4	+15.4	+2.2	+16.5
Irradiance + RMSE	−25.2	+2.6	−15.8	−23.4	−1.1	−24.1
R, C × 0.8	+4.0	−0.3	+1.3	+2.2	+4.9	+2.1
R, C × 1.2	−1.0	+0.5	−1.0	−1.0	−1.3	−0.8
With solar gains	−1.5	+0.8	−0.8	+0.2	+5.8	+1.0
Variable COP	−11.4	−2.1	−5.1	−3.7	−3.6	−4.3

The ex post results show how the forecast errors propagate into the day-ahead schedule. An error of one RMSE in the outdoor temperature changes the daily cost of S_2 by about ±8% and its emissions by about ±9%, through the air-conditioner and water-heater consumption, while an error of one RMSE in irradiance, applied to every daylight hour, changes the cost by +15% to −21% through the PV generation. The comfort index does not change, because it depends only on the schedule. These deviations are upper bounds of the error of a single day, since the RMSE shift is applied with the same sign to all hours, whereas actual forecast errors partly cancel over the day. When the optimization is repeated with the perturbed forecasts, the representative solutions change by similar amounts; i.e., re-optimizing does not compensate for a biased forecast. A tariff variation of ±20% changes the cost by −14% to +12%, with little effect on comfort and emissions; i.e., the schedules are robust to the price level. The thermal parameters (±20%), the solar gains, and the variable COP change the cost by less than 4% ex post; with the variable COP, the air-conditioner energy of S_2 falls by 19.6%, confirming that the constant rated COP is a conservative assumption, while the solar gains increase it by only 1.2%, because the air conditioners operate at night. Differences of 2–5% in the re-optimized results, such as the changes of comfort in the tariff scenarios, are within the run-to-run variability of the algorithm (Section 2.8).

4. Discussion and Practical Implications

4.1. Regulatory and Economic Alignment Under Brazilian Law 14300/2022

The transition from net-metering to tariff-based grid remuneration under Brazilian Law 14300/2022 has introduced progressive grid access charges on distributed generation. In this regulatory context, the traditional operational paradigm of maximizing solar energy export is no longer financially viable. The proposed HEMS demonstrates that coupling rooftop PV with EV storage and flexible load shifting increases self-consumption to 94.0%, against 50.7% in the non-optimized household, effectively insulating prosumers from wire tariff amortization costs. Furthermore, under the White Tariff, the 2.12:1 ratio between peak (BRL 1.42/kWh) and off-peak (BRL 0.67/kWh) rates provides a strong price signal, enabling the HEMS to prioritize EV charging during periods of excess generation or off-peak hours without accelerating battery degradation.

4.2. Distribution Grid Peak Shaving and Asset Longevity

From a distribution system operator (DSO) perspective, uncoordinated residential EV charging and simultaneous peak-hour appliance usage threaten low-voltage distribution transformers with severe thermal overload and voltage degradation. The results in Section 3 demonstrate that the knee-point policy (S_2) reduces the maximum grid import within the peak tariff block from 1.67 kW (both the maximum-comfort schedule S_3 and the non-optimized reference S_0) to 0.54 kW, a reduction of 67.4%, and avoids the 5.1 kW import caused by the uncontrolled EV charging of S_0 at midday. However, the EV charging that is not supplied by PV is deferred to the first off-peak interval after the peak block, where S_2 imports 4.99 kW; if many households adopted the same strategy, this post-peak rebound would create a new feeder peak, so a coordinated deployment would require a power cap or a staggered charging window in the optimization. By acting as a decentralized flexibility resource, the proposed framework can mitigate substation congestion, defer capital-intensive grid reinforcement, and enhance the hosting capacity of residential distribution feeders, provided that the post-peak rebound is managed.

4.3. Methodological Limitations

Several specific simplifications delimit the scope of the present findings. First, solar radiation heat gains through building fenestration were omitted from the lumped RC envelope model; while the literature confirms that outdoor air temperature governs the primary thermal response [13], heavily glazed architectural designs may require explicit radiative heat transfer terms; in the case studied, including them changes the air-conditioner energy of S_2 by 1.2% and its cost by 0.2% (Section 3.12), because the air conditioners operate at night. Second, the comfort matrix was constructed from aggregated national survey statistics [19] rather than real-time smart meter telemetry from an individual household; however, the framework seamlessly ingests personalized usage data. Third, the simulation evaluates a representative day-ahead horizon; multi-seasonal continuous operational testing with rolling-horizon model predictive control (MPC) will further consolidate long-term battery degradation and cycling economics. Representative summer and winter days would change the air-conditioning demand, the shower inlet temperature, and the PV output, and therefore the absolute costs and emissions; extending the simulations to these days is part of future work.

Fourth, the air conditioner uses a constant rated COP. Because the rating condition (35 °C outdoors) is hotter than the outdoor temperatures in the hours of operation (19.7–21.0 °C), this assumption tends to overestimate the AC consumption; with a COP that varies by 25% between 20 and 35 °C, the AC energy of S_2 falls by 19.6% and its daily cost by 3.6% (Section 3.12). Part-load effects were not modeled. This error is of a different

nature from the difference of Table 10, which refers to the water heater and not to the air conditioner.

Fifth, the emission factor $E_f(i)$ is an average hourly profile of a representative day of 2023 (direct intensity)—not the marginal intensity of each hour. In the average profile, the evening hours have the lowest intensity, whereas the marginal plant in the evening ramp of the Brazilian grid is typically a thermal plant. With marginal factors, the evening imports of S_4 would therefore be penalized, and the emission reduction of S_4 relative to S_1, which is small in the present results (1.0–2.2%), could change sign; the reduction relative to S_0 and S_3, which comes mainly from the self-consumption of the PV surplus, would be preserved. The emission results should therefore be read as attributional.

Sixth, the EV charger is unidirectional (G2V). V2H operation would allow the EV battery to supply the evening load and could further reduce the evening import; it was not considered because it requires a bidirectional charger and increases battery cycling, and this is left for future work.

Finally, the forecasting errors of Section 3.1 affect the day-ahead schedule; their effect on cost, comfort, and emissions was quantified in Section 3.12 (about $\pm$8% of the daily cost for one RMSE of temperature), and in a real deployment, it would be further reduced by a rolling-horizon re-optimization with updated forecasts. The envelope parameters adopted make the wall layers weakly coupled to the indoor air so that the heat exchange of the rooms occurs mainly through the glazing; detailed envelope data of a specific dwelling would be needed to quantify the pre-cooling potential of the wall mass.

5. Conclusions

This paper proposed an advanced multi-objective home energy management system that integrates the NSGA-III evolutionary algorithm with physics-based building envelope and TCL models, deep-learning stacking meteorological forecasting, and electric vehicle battery storage (EVESS). The main conclusions are summarized as follows:

1. **Comprehensive Multi-Objective Trade-offs:** The multi-objective framework establishes clear Pareto trade-offs among cost, comfort, and emissions. Under the Brazilian White Tariff (TOU-1), the knee point solution (S_2) reduces the daily cost by 27.1% (BRL 185/month) and the emissions by 28.3% with respect to a non-optimized household (S_0) while keeping 90.2% of the theoretical maximum comfort. Within the optimized front, S_2 retains 91.8% of the comfort of the maximum-comfort schedule (S_3) at only BRL 0.49/day above the minimum-cost policy (S_1), which saves 22.2% relative to S_3. Under the more segmented TOU-2, S_2 saves 20.3% relative to S_0.
2. **Environmental Decarbonization and Peak Mitigation:** The minimum-emission policy (S_4) reduces daily emissions to about 1.09 $kgCO_2eq$/day (13.2% below S_3 under TOU-1 and 18.0% under TOU-2, and about 32% below S_0), mostly through the self-consumption of the PV surplus, which also reduces cost. Coordinated EV charging and load scheduling reduce the maximum grid import in the peak tariff block by 67% and raise PV self-consumption from 50.7% to 94.0%, which is in alignment with Brazilian Law 14300/2022; the deferred EV charging, however, creates a post-peak import of about 5 kW that must be limited if the strategy is adopted at scale.
3. **High-Fidelity Physical Coupling:** Incorporating a 4R3C building thermal network and a thermodynamic water heater model directly into the optimization fitness function reflects weather-driven load dynamics: for the shower, a constant-power model would overestimate the daily energy by 42.2%, and an error of one RMSE in the temperature forecast changes the daily cost by about $\pm$8%, which shows the importance of accurate weather forecasts for day-ahead scheduling.

4. **Algorithm choice:** For this three-objective problem, NSGA-III and NSGA-II produced statistically equivalent fronts under the same computational budget, NSGA-II being about five times faster.

Future research will extend this framework toward multi-zone building thermal dynamics, rolling-horizon model predictive control (MPC) with real-time feedback compensation, and vehicle-to-grid (V2G) and vehicle-to-home (V2H) operation, ancillary service provision for low-voltage distribution networks, representative summer and winter days, hourly marginal emission factors, and the co-optimization of load scheduling with passive envelope measures such as insulation and phase change composites, whose effect can be represented by the capacitances and resistances of the RC model.

Author Contributions: Conceptualization, A.F.N.A., H.R.d.O.R. and R.F.; methodology, A.F.N.A. and R.F.; software, A.F.N.A. and R.F.; validation, A.F.N.A., C.R.C., H.R.d.O.R. and R.F.; formal analysis, A.F.N.A. and R.F.; investigation, A.F.N.A. and R.F.; writing—original draft preparation, C.R.C., J.F.F., L.F.S.A., H.R.d.O.R. and R.F.; writing—review and editing, C.R.C., J.F.F., L.F.S.A., H.R.d.O.R. and R.F.; supervision, H.R.d.O.R. and J.F.F. All authors have read and agreed to the published version of the manuscript.

Funding: This research was financed in part by the Coordenação de Aperfeiçoamento de Pessoal de Nível Superior-Brasil (CAPES)—Finance Code 001. FAPES 2022-BWBR2, 2024-1FNPM and 2026-6WKKX. In addition to CNPQ 311894/2025-9.

Institutional Review Board Statement: Not applicable.

Informed Consent Statement: Not applicable.

Data Availability Statement: The simulation data and the MATLAB implementation are available from the corresponding author upon reasonable request.

Conflicts of Interest: The authors declare no conflicts of interest.

Nomenclature

Abbreviations

AB, AS	Air conditioner of the bedroom and of the suite
AC	Air conditioner
CD	Clothes dryer
CF, FF	Ceiling fan, floor fan
COP	Coefficient of performance
DW	Dishwasher
EI	Electric iron
EO	Electric oven
ES	Electric shower (tankless water heater)
EV	Electric vehicle
EVESS	EV energy storage system
G2V	Grid-to-vehicle
HEMS	Home energy management system
HV	Hypervolume indicator
4R3C	Four-resistance, three-capacitance network
WM	Washing machine
LSTM	Long Short-Term Memory network
MAE	Mean absolute error
MAPE	Mean absolute percentage error
NSGA	Non-dominated Sorting Genetic Algorithm
PV	Photovoltaic
RC	Resistance–capacitance
RMSE	Root mean squared error

SH	Smart home
SIN	Brazilian National Interconnected System
SOC, SOH	State of charge, state of health
TCL	Thermostatically controlled load
TCN	Temporal Convolutional Network
TFT	Temporal Fusion Transformer
TOU	Time-of-use (tariff)
V2G, V2H	Vehicle-to-grid, vehicle-to-home
Indices and sets	
i	Hourly interval, $i = 1, \ldots, N_i$ ($N_i = 24$)
j	Appliance index
N_c, N_t	Number of shiftable and thermal appliances
N_{nc}	Number of non-controllable appliances
Parameters and variables	
c_d, n	Cycle duration (h), number of daily cycles
p_{cd}	Fraction of the operating hour at nominal power
c_e	Daily operation cost (BRL)
c_{con}, c_{inj}	Consumption cost, injection revenue (BRL)
c_{deg}, c_p	Battery degradation cost, SOC penalty (BRL)
c_p	Specific heat of water (J/kg·°C), Equations (8)–(20) only
C_a	Thermal capacitance of indoor air (J/K)
$C_{m,in}$, $C_{m,out}$	Capacitances of inner and outer wall layers (J/K)
C_{bat}	EV battery capacity (kWh)
C_{inv}	Battery replacement cost (BRL/kWh)
E_{CO_2}	Daily emissions ($kgCO_2eq$)
$E_f(i)$	Grid emission factor ($kgCO_2eq/kWh$)
$f(i,j)$	Usage probability (comfort matrix)
$s_p(i,j)$	Binary schedule of appliance j
P_{ar}, P_s	Electrical power of AC and shower (W)
P_t	Thermal-load power, $P_{ar} + P_s$ (W)
P_c, P_{nc}	Shiftable and non-controllable power (W)
P_h	Total smart-home demand (W)
P_{pv}	PV generation (W)
P_{net}, P_{grid}	Net and grid exchange power (W)
P_{bat}, P_{ope}	Charger power, EV driving power (W)
P_{cd}	Charging fraction (decision variable)
Q_{total}	Thermal power extracted by the AC (W)
Q_s	Thermal power of the shower heater (W)
R_{in}, R_{out}	Convective resistances (K/W)
R_m, R_w	Wall and window resistances (K/W)
T_a, T_{amb}	Indoor-air and outdoor temperatures (°C)
$T_{m,in}$, $T_{m,out}$	Inner/outer wall temperatures (°C)
T_{set}	AC set-point (°C)
U_c	Comfort index (appliance-timing preference)
Δt	Time step (h)
η_{ch}, η_{rt}, η_s	Charging, round-trip and heater efficiencies
σ	Battery self-discharge rate
SOC_{min}, SOC_{max}	SOC limits

References

1. Varghese, B.K.; Das, N.; Ray, B.; Mazid, A.M.; Jahan, I.; Nur-E-Alam, M. Optimisation algorithms used in home energy management systems: A review. *Energy Build.* **2025**, *347*, 116338. [CrossRef]
2. Carrera, L.A.I.; Ramirez-Ceballos, J.C.; Molina-Santana, E.; Velásquez, F.A.C.; Mayra, C.F.; Álvarez-Alvarado, J.M.; Rodríguez-Reséndiz, J. Integration of energy management and efficiency system for buildings with zero carbon emissions: A case of study. *IEEE Access* **2024**, *12*, 64237–64251. [CrossRef]

3. Agência Nacional de Energia Elétrica (ANEEL). *Normative Resolution No. 1059 of 7 February 2023: Rules for Micro- and Mini-Distributed Generation Under Law 14300/2022*; ANEEL: Brasília, Brazil, 2023. Available online: https://www2.aneel.gov.br (accessed on 13 January 2026).
4. Mariano-Hernández, D.; Hernández-Callejo, L.; Zorita-Lamadrid, A.; Duque-Pérez, O.; Santos García, F. A review of strategies for building energy management system: Model predictive control, demand side management, optimization, and fault detect & diagnosis. *J. Build. Eng.* **2021**, *33*, 101692. [CrossRef]
5. Zhao, C.; Wu, X.; Hao, P.; Wang, Y.; Zhou, X. Machine learning for optimal net-zero energy consumption in smart buildings. *Sustain. Energy Technol. Assess.* **2024**, *64*, 103664. [CrossRef]
6. Saif, O.; Elazab, R.; Daowd, M. Smart home energy management for sustainable socioeconomic development in Egyptian households. *Sci. Rep.* **2026**, *16*, 5654. [CrossRef]
7. Bianchini, G.; Casini, M.; Pepe, D.; Vicino, A.; Zanvettor, G. An integrated model predictive control approach for optimal HVAC and energy storage operation in large-scale buildings. *Appl. Energy* **2019**, *240*, 327–340. [CrossRef]
8. Jiang, X.; Wu, L. A residential load scheduling based on cost efficiency and consumer's preference for demand response in smart grid. *Electr. Power Syst. Res.* **2020**, *186*, 106410. [CrossRef]
9. Nezhad, A.E.; Rahiminejad, A.; Gadsden, S.A. Home energy management system for smart buildings with inverter-based air conditioning system. *Int. J. Electr. Power Energy Syst.* **2021**, *133*, 107230. [CrossRef]
10. Shaikh, P.H.; Nor, N.B.M.; Nallagownden, P.; Elamvazuthi, I.; Ibrahim, T. Intelligent multi-objective control and management for smart energy efficient buildings. *Int. J. Electr. Power Energy Syst.* **2016**, *74*, 403–409. [CrossRef]
11. Empresa de Pesquisa Energética (EPE). *Atlas da Eficiência Energética Brasil 2023: Relatório de Indicadores*; EPE: Rio de Janeiro, Brazil, 2023. Available online: https://www.epe.gov.br (accessed on 11 December 2024).
12. Li, Y.; O'Neill, Z.; Zhang, L.; Chen, J.; Im, P.; DeGraw, J. Grey-box modeling and application for building energy simulations—A critical review. *Renew. Sustain. Energy Rev.* **2021**, *146*, 111174. [CrossRef]
13. Wang, C.; Ji, J.; Yang, H. Day-ahead schedule optimization of household appliances for demand flexibility: Case study on PV/T powered buildings. *Energy* **2024**, *289*, 130042. [CrossRef]
14. Fiorotti, R.; Fardin, J.F.; Rocha, H.R.O.; Rua, D.; Lopes, J.A.P. Day-ahead optimal scheduling considering thermal and electrical energy management in smart homes with photovoltaic–thermal systems. *Appl. Energy* **2024**, *374*, 124070. [CrossRef]
15. Fiorotti, R.; Fardin, J.F.; Rocha, H.R.O.; Rueda-Medina, A.C.; Pantaleo, A.M.; Nasab, M.R.; Bruno, S. A new approach for HEMS to optimize cost, emissions and comfort through a smart integration of V2G, load scheduling, and PVT generation. *Energy Build.* **2026**, *356*, 117094. [CrossRef]
16. Luo, Z.; Peng, J.; Yin, R. Many-objective day-ahead optimal scheduling of residential flexible loads integrated with stochastic occupant behavior models. *Appl. Energy* **2023**, *347*, 121348. [CrossRef]
17. Fiorotti, R.; Fardin, J.F.; Rocha, H.R.O.; Rueda-Medina, A.C.; Zanotelli, T.; Bruno, S. Optimizing Home Energy Systems with Electric Vehicles for Sustainable Living. In Proceedings of the 2024 IEEE International Humanitarian Technologies Conference (IHTC), Bari, Italy, 27–30 November 2024; pp. 1–7.
18. Deb, K.; Jain, H. An evolutionary many-objective optimization algorithm using reference-point-based nondominated sorting approach, Part I: Solving problems with box constraints. *IEEE Trans. Evol. Comput.* **2014**, *18*, 577–601. [CrossRef]
19. Centrais Elétricas Brasileiras S.A. (Eletrobras). *Pesquisa de Posse e Hábitos de Uso de Equipamentos Elétricos na Classe Residencial: PPH 2019*; Eletrobras/Procel: Rio de Janeiro, Brazil, 2019. Available online: https://www.procel.gov.br (accessed on 22 January 2026).
20. Ministério do Meio Ambiente. *Projeteee—Projetando Edificações Energeticamente Eficientes*; MMA: Brasília, Brazil. Available online: https://www.projeteee.mma.gov.br (accessed on 6 March 2026).
21. Fiorotti, R.; Fardin, J.F.; Rocha, H.R.O.; Rueda-Medina, A.C.; Coutinho, C.R.; Zanotelli, T.; Bruno, S. Integration of day-ahead HEMS planning with MPC for real-time operation of smart homes with PV and V2G. *IEEE Trans. Ind. Appl.* **2026** , 1–12. [CrossRef]
22. Laicane, I.; Blumberga, D.; Blumberga, A.; Rosa, M. Reducing household electricity consumption through demand side management: The role of home appliance scheduling and peak load reduction. *Energy Procedia* **2015**, *72*, 222–229. [CrossRef]
23. Heleno, M.; Matos, M.A.; Lopes, J.A.P. Availability and flexibility of loads for the provision of reserve. *IEEE Trans. Smart Grid* **2014**, *6*, 667–674. [CrossRef]
24. Abreu, C.; Rua, D.; Machado, P.; Lopes, J.A.P.; Heleno, M. Advanced energy management for demand response and microgeneration integration. In Proceedings of the Power Systems Computation Conference (PSCC), Dublin, Ireland, 11–15 June 2018; pp. 1–7.
25. Paterakis, N.G.; Erdinç, O.; Bakirtzis, A.G.; Catalão, J.P.S. Optimal household appliances scheduling under day-ahead pricing and load-shaping demand response strategies. *IEEE Trans. Ind. Inform.* **2015**, *11*, 1509–1519. [CrossRef]
26. Erdinç, O.; Paterakis, N.G.; Mendes, T.D.P.; Bakirtzis, A.G.; Catalão, J.P.S. Smart household operation considering bi-directional EV and ESS utilization by real-time pricing-based demand response. *IEEE Trans. Smart Grid* **2015**, *6*, 1281–1291. [CrossRef]
27. Wang, C.; Zhou, Y.; Jiao, B.; Wang, Y.; Liu, W.; Wang, D. Robust optimization for load scheduling of a smart home with photovoltaic system. *Energy Convers. Manag.* **2015**, *102*, 247–257. [CrossRef]

28. Rajalingam, S.; Malathi, V. HEM algorithm based smart controller for home power management system. *Energy Build.* **2016**, *131*, 184–192. [CrossRef]
29. Shakeri, M.; Shayestegan, M.; Reza, S.M.S.; Yahya, I.; Bais, B.; Akhtaruzzaman, M.; Sopian, K.; Amin, N. Implementation of a novel home energy management system (HEMS) architecture with solar photovoltaic system as supplementary source. *Renew. Energy* **2018**, *125*, 108–120. [CrossRef]
30. Gheouany, S.; Ouadi, H.; El Bakali, S. Hybrid-integer algorithm for a multi-objective optimal home energy management system. *Clean Energy* **2023**, *7*, 375–388. [CrossRef]
31. Dehghani, M.; Bornapour, S.M. Smart homes energy management: Optimal multi-objective appliance scheduling model considering electrical energy storage and renewable energy resources. *Heliyon* **2025**, *11*, e42417. [CrossRef]
32. Terci Flores, J.; Celeste, W.C.; Coura, D.J.C.; Rissino, S.D.; Rocha, H.R.O.; Moraes, R.E.N. Demand planning in smart homes. *IEEE Lat. Am. Trans.* **2016**, *14*, 3247–3255. [CrossRef]
33. Kuznik, F.; David, D.; Johannes, K.; Roux, J.-J. A review on phase change materials integrated in building walls. *Renew. Sustain. Energy Rev.* **2011**, *15*, 379–391. [CrossRef]
34. Hu, J.; Zou, M.; Wang, J.; Zou, S.; Liu, Y.; Ma, Y.; Chen, W.; Li, Q.; He, Y.; Jiang, X.; et al. Multifunctional anisotropic PEG/P-N co-doped rGO aerogel phase change composites: Tuning phonon transport for smart thermal and EMI management. *Chem. Eng. J.* **2026**, *535*, 175841. [CrossRef]
35. Rocha, H.R.O.; Honorato, I.H.; Fiorotti, R.; Celeste, W.C.; Silvestre, L.J.; Silva, J.A.L. An Artificial Intelligence based scheduling algorithm for demand-side energy management in smart homes. *Appl. Energy* **2021**, *282*, 116145. [CrossRef]
36. Fiorotti, R.; Yahyaoui, I.; Rocha, H.R.O.; Honorato, I.; Silva, J.; Tadeo, F. Demand planning of a nearly zero energy building in a PV/grid-connected system. *Renew. Energy Focus* **2023**, *45*, 220–233. [CrossRef]
37. Abdel-Nasser, M.; Mahmoud, K. Accurate photovoltaic power forecasting models using deep LSTM-RNN. *Neural Comput. Appl.* **2019**, *31*, 2727–2740. [CrossRef]
38. Lim, S.-C.; Huh, J.-H.; Hong, S.-H.; Park, C.-Y.; Kim, J.-C. Solar power forecasting using CNN-LSTM hybrid model. *Energies* **2022**, *15*, 8233. [CrossRef]
39. Peng, F.; Tang, X.; Xiao, M. Attention-enhanced CNN-LSTM with spatial downscaling for day-ahead photovoltaic power forecasting. *Sensors* **2026**, *26*, 593. [CrossRef]
40. de Lima, T.D.; Faria, P.; Vale, Z. Optimizing home energy management systems: A mixed integer linear programming model considering battery cycle degradation. *Energy Build.* **2025**, *329*, 115251. [CrossRef]
41. Huy, T.H.B.; Dinh, H.T.; Vo, D.N.; Kim, D. Real-time energy scheduling for home energy management systems with an energy storage system and electric vehicle based on a supervised-learning-based strategy. *Energy Convers. Manag.* **2023**, *292*, 117340. [CrossRef]
42. Deb, K.; Pratap, A.; Agarwal, S.; Meyarivan, T. A fast and elitist multiobjective genetic algorithm: NSGA-II. *IEEE Trans. Evol. Comput.* **2002**, *6*, 182–197. [CrossRef]
43. Ishibuchi, H.; Tsukamoto, N.; Nojima, Y. Evolutionary many-objective optimization: A short review. In Proceedings of the 2008 IEEE Congress on Evolutionary Computation (CEC), Hong Kong, China, 1–6 June 2008; pp. 2419–2426.
44. Hochreiter, S.; Schmidhuber, J. Long short-term memory. *Neural Comput.* **1997**, *9*, 1735–1780. [CrossRef] [PubMed]
45. Graves, A.; Schmidhuber, J. Framewise phoneme classification with bidirectional LSTM and other neural network architectures. *Neural Netw.* **2005**, *18*, 602–610. [CrossRef]
46. Bai, S.; Kolter, J.Z.; Koltun, V. An empirical evaluation of generic convolutional and recurrent networks for sequence modeling. *arXiv* **2018**, arXiv:1803.01271 .
47. Lim, B.; Arık, S.Ö.; Loeff, N.; Pfister, T. Temporal Fusion Transformers for interpretable multi-horizon time series forecasting. *Int. J. Forecast.* **2021**, *37*, 1748–1764. [CrossRef]
48. Wolpert, D.H. Stacked generalization. *Neural Netw.* **1992**, *5*, 241–259. [CrossRef]
49. *ISO 5151:2017*; Non-Ducted Air Conditioners and Heat Pumps—Testing and Rating for Performance. ISO: Geneva, Switzerland, 2017.
50. Incropera, F.P.; DeWitt, D.P.; Bergman, T.L.; Lavine, A.S. *Fundamentals of Heat and Mass Transfer*, 7th ed.; LTC: Rio de Janeiro, Brazil, 2014.
51. Sangoi, J.M.; Ghisi, E. Energy efficiency of water heating systems in single-family dwellings in Brazil. *Water* **2019**, *11*, 1068. [CrossRef]
52. Wu, Y.; Liu, Z.; Li, B.; Liu, J.; Zhang, L. Energy management strategy and optimal battery capacity for flexible PV-battery system under time-of-use tariff. *Renew. Energy* **2022**, *200*, 558–570. [CrossRef]
53. Electricity Maps. Brazil 2023 Carbon Intensity Data (Version 27 January 2025). 2025. Available online: https://www.electricitymaps.com (accessed on 20 September 2026).
54. Zitzler, E.; Thiele, L. Multiobjective evolutionary algorithms: A comparative case study and the strength Pareto approach. *IEEE Trans. Evol. Comput.* **1999**, *3*, 257–271. [CrossRef]

Disclaimer/Publisher's Note: The statements, opinions and data contained in all publications are solely those of the individual author(s) and contributor(s) and not of MDPI and/or the editor(s). MDPI and/or the editor(s) disclaim responsibility for any injury to people or property resulting from any ideas, methods, instructions or products referred to in the content.